



# Application of periwinkle shell for the synthesis of calcium oxide nanoparticles and in the remediation of Pb<sup>2+</sup>-contaminated water

Nnabuk Okon Eddy<sup>1</sup> · Rajni Garg<sup>2</sup> · Richard Alexis Ukpe<sup>3</sup> · Paul Ocheje Ameh<sup>4</sup> · Rishav Garg<sup>5</sup> · Musa Runde<sup>6</sup> · Iliya Dimas Kwanchi<sup>6</sup> · Saikh Mohammad Wabaidur<sup>7</sup> · Sikandar Aftab<sup>8</sup> · Raphael Ogbodo<sup>9</sup> · Augustine Odiba Aikoye<sup>1</sup> · Masoom Siddiqu<sup>8,10</sup>

Received: 20 October 2023 / Revised: 25 December 2023 / Accepted: 3 January 2024  
© The Author(s), under exclusive licence to Springer-Verlag GmbH Germany, part of Springer Nature 2024

## Abstract

The need to reduce the cost of production of highly demanding nanoparticles is receiving some challenges, especially the availability of the needed raw materials. Calcium oxide nanoparticles are one of the most useful nanoparticles because of their unique properties that favour environmental applications. In this study, costless raw materials (periwinkle shells) of raw materials for the production of calcium oxide nanoparticles using a sol–gel method of synthesis. The nanoparticles were characterized using XRD, FT-IR, UV visible spectrophotometer, SEM, BET, and ICP instrumentation. Information obtained from the characterization showed that the material has a band gap of 4.12 eV, average crystallite size of 18 nm, BET surface area 220.11 m<sup>2</sup>/g, pore volume of 8.43 cc/g and mesoporous property defined by average porosity of 59%, and pore diameter of 3.02 nm. The XRD peaks. The XRD spectrum of the synthesized product showed a principal diffraction peak at 34.2163° with other peaks that confirmed CaO nanoparticle phases. The specific surface area deduced from the XRD spectrum (average = 98 m<sup>2</sup>/g) was lower than that value obtained from the nitrogen adsorption study. Based on the characters observed for the nanoparticles, they were applied for adsorption removal of lead under different conditions (including pH, [Pn<sup>2+</sup>], time, and adsorbent dosage), and the evaluated adsorption efficiency was 99 g/mg while the optimum efficiency of 98% was observed at the normal experimental condition and 100% under photoactivated adsorption. The nanoparticles showed high recyclability (< 90%) and their tendency to adsorb increases with a decrease in temperature. Tests conducted on different kinetic and adsorption models support the fitness of pseudo-second-order kinetic, liquid film diffusion, Freundlich, Halsey, and Elovich adsorption models. The impact of the interaction of the tested factors on adsorption was investigated using response surface analysis, and it was observed that the optimum adsorption efficiency can be reduced when all the factors are combined. Therefore, an optimum efficiency of 80% at an adsorbent dosage of 0.5, time = 75 min, temperature = 318 K, and concentration of 250% was statistically significant.

**Keywords** Lead (II) toxicity · Water quality · Restoration · Adsorption · CaO–NPs

## 1 Introduction

In current times, the literature is highly dominated by reports on the toxicity of heavy metal ions in water due to the established potential toxic impact of these metal ions on public health [1]. Heavy metals such as lead are persistent and cannot easily be destroyed by biological organisms [2]. Unfortunately, one of the easiest routes for heavy metals to enter the environment is the aqueous media [3]. The after-effect of heavy metal ions' intrusion into the aquatic environment is interference with the global demand for potable water and the

increasing risk of health challenges. Consequently, the associated problems are expanding daily, especially when considering the usefulness of water for the survival of living organisms, irrigation, agricultural activities, and various domestic and industrial applications [4]. The beneficial roles of water can deeply be limited by the presence of heavy metal contaminants and can progress further to initiate toxic impacts ranging from mild effects to death. Much has been reported on the short, medium, and long-term toxicity impacts of lead ions, but the terminal effect is dead [5–7].

Given their confirmed poisonous nature, some technologies have been developed to enhance the withdrawal of lead ions from water, such as adsorption, dialysis, and

Extended author information available on the last page of the article

bioremediation [8, 9]. However, some of the major challenges associated with the achievement of optimum efficiency from most of these technologies are high materials and implementation costs, scarcity of raw materials, materials limitation, lack of or insufficient power supply, secondary waste management, etc. [10, 11].

Adsorption is one of the widely accepted methods that can easily be modelled towards the achievement of excellent efficiency through materials selection, eco-friendly practices, and limited input of resources [12]. There are different materials suitable as adsorbents for the removal of lead (II) from an aqueous solution, such as plant and animal materials [13], inorganic materials [14], organic and inorganic polymers [15], and synthetic materials [16]. However, nanoparticles have remarkable advantages over several classical counterparts because they possess high thermally and mechanical stability, porosity [17], reusability [18], and high adsorption surface area due to their nano sizes [19]. Also, efforts are currently on the way to harness the outstanding advantages offered by nanoparticles towards the enhancement of adsorption for the improvement of the overall quality of wastewater instead of the removal of heavy metal alone [20]. Probably some precursors for the synthesis of nanoparticles are relatively toxic and may constitute secondary toxicity [21]. The cost of synthesis may be extremely high when subjected to cost–benefit analysis, and some of the raw materials or the required instrumentation are not easily accessible, thereby defiling the required environmental and economic protocols. Cost–benefit analysis can easily be achieved through the utilization of waste materials that do not have immediate benefit or usefulness to man and need to be disposed of. Some solid waste such as shells of crustaceans and bones of animals have chemical contents that can be converted to precursors for nanomaterials synthesis. For example, Essien et al. [22] successfully synthesized calcium oxide nanoparticles (CaO–NP) from snail shells for the adsorption removal of amoxicillin water and the results obtained indicated almost complete removal efficiency. In our research group, we have obtained good surface properties for calcium oxide nanoparticles synthesized from oyster shells, and further applications in the removal of contaminants indicated excellent removal efficiencies for methyl orange [23], procaine penicillin [24], bromocresol green [25], and methylene blue [26]. Crab [27] and mussel [28] shells have also been found to be excellent precursors for the synthesis of CaO–NP, and their adsorption properties were properly affirmed based on the evaluated properties. A critical examination of the highlighted and other crustacean shells indicates that they are rich in  $\text{CaCO}_3$ , which can be easily converted to CaO–NP.

Given the yet-to-be-developed procedures in the management of periwinkle shell wastes, the high  $\text{CaCO}_3$  content and the increasing demand for nontoxic raw materials (such as

calcium oxide nanoparticles) for the treatment of industrial and other forms of effluence against lead toxicity, the present study is aimed at converting  $\text{CaCO}_3$  (in periwinkle shell) to CaO nanoparticles (CaO–NPs) for immediate application in the adsorption removal of Pb(II) from aqueous solution. To fully achieve this aim, the study shall also assess the possibility of using and re-using the CaO–NPs and the influence of the adsorption process on the physicochemical quality of the water.

## 2 Materials and methods

### 2.1 Synthesis of CaO–NPs

Periwinkle shells were used as precursors for the synthesis of CaO–NPs. In the periwinkle processing zone (where the samples were collected), the routine practice is to remove the flesh and dispose of the shell as solid waste. The collected samples were washed, dried, and crushed to powder form using an electric motor connected to a crusher. The grounded samples (with reduced particle size) were reacted with 2 M HCl to convert the  $\text{CaCO}_3$  to  $\text{CaCl}_2$ . The formed sol was reacted with a 50% solution of NaOH to yield  $\text{Ca}(\text{OH})_2$  gel. The system was allowed to stay for 12 h after which it was thoroughly washed with distilled water, dried to constant weight, and calcined at 800 °C for 2 h.

### 2.2 Characterization

The prepared CaO–NPs were characterized using an X-ray diffractometer, Fourier transformed infrared (FT-IR), Braeuner-Emmett-Teller analyzer (BET), UV–visible spectrophotometer, and scanning electron microscope. All measurements for the concentration of Pb(II) were done using inductive coupling plasma (ICP).

### 2.3 Adsorption experiment

Batch adsorption experiments were implemented using the method widely reported in the literature [29]. The experimental steps started with the preparation of various concentrations of lead (II) (10, 20, 30, and 40 ppm) using  $\text{Pb}(\text{NO}_2)_2$ . The influence of concentrations was investigated using the listed concentrations and the time involved was 60 min. The contribution of the period of contact, pH, the dosage of CaO–NPs, and temperatures to the removal of Pb(II) were also investigated by varying these factors over reasonable ranges. In each case, the equilibrium amount of the metal on removed by the adsorbent ( $Q_e$ ) and the percentage removal was computed using Eq. 1 and 2 [30].

$$Q_e = \frac{V}{m} \times (C_0 - C_e) \quad (1)$$

$$\% Pb^{2+} \text{ removed} = \frac{(C_0 - C_e)}{C_0} \quad (2)$$

The initial or intake and outlet concentrations are represented as  $C_0$  and  $C_e$  respectively in the above equations.

## 2.4 Process optimization and interaction

Design expert 13 was used to design a 2-by-4, fifteen-sample runs consisting of various combinations of temperature, concentration, adsorbent dosage, and time. Analyses were performed to establish interaction parameters for various combinations of the listed parameters and to establish the optimum conditions associated with optimum adsorption efficiency.

## 3 Results and discussion

### 3.1 Characterization of adsorbent

The particle size, surface area, adsorption energy, porosity, and other pore parameters of the nanocomposite (CaO–NPs) were evaluated using Bruaner-Emmett-Teller (BET) and various isotherms developed from data associated with the nitrogen adsorption (such as multiple BET) were employed to evaluate the pore parameters for the adsorbent.

The multi BET (M-BET) model can be represented as a linear shown in Eq. 3 [31],

$$\frac{1}{N[(P_0/P) - 1]} = \frac{1}{N_m} + \frac{C - 1}{N_m C} \left( \frac{P}{P_0} \right) \quad (3)$$

In the above Eq. (3),  $N$  represents the amount of  $N_2$  adsorbed at a pressure,  $P$ , giving an initial pressure,  $P_0$ ,  $N_m$  stands for the adsorption capacity of the monolayer, and  $C$  is a constant, whose value is related to the heat capacity,  $C = [q_{ads} - q_{cond}]/RT$ . Also,  $q_{ads}$  is the adsorption heat while  $q_{cond}$  is the heat of condensation of the adsorbate. The M-BET surface area was evaluated from the slope and intercept of the M-BET plot (Fig. 1) [32], and the values obtained are recorded in Table 1. Other pore parameters (also recorded in Table 1) were also obtained from other isotherms, including Dubinin-Ashtakov (D-A), Barreett-Joyner-Halenda (B-JH), Dubinin-Radushkevich (D-R), Density functional theory (DFT) and Horvath-Kawazoe (HK) methods. The measured surface area showed the lowest from the DFT model (54.32  $m^2/g$ ) while the D-H model revealed the highest (265.14  $m^2/g$ ). Also, the pore volume parameters obtained from the various models (excluding M-BET) showed a range

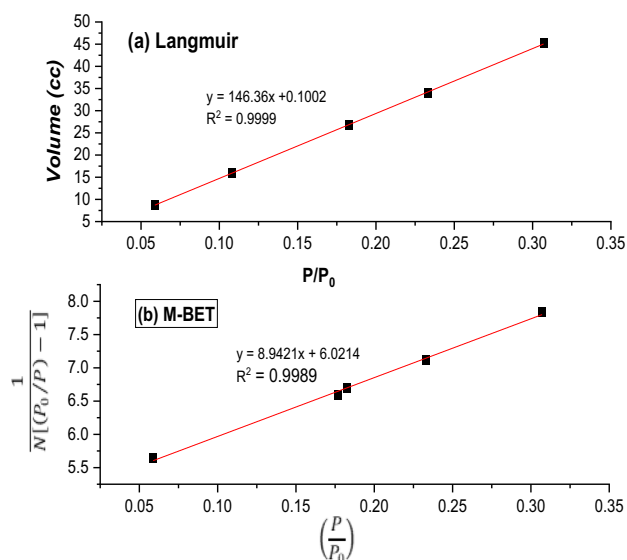


**Fig. 1** Langmuir and M-BET isotherms for  $N_2$  adsorption by CaO–NPs

**Table 1** Pore parameters for the CaO–NPs

Model	Surface area ( $m^2/g$ )	Pore volume (cc/g)	Pore diameter (nm)	Surface area: Pore volume ( $m^{-1}$ )
M-BET	265.14	-	-	-
B-JH	246.82	13.02	2.030	$1.90 \times 10^8$
D-H	280.24	13.04	2.342	$2.15 \times 10^7$
D-R	254.01	8.93	5.923	$2.84 \times 10^7$
DFT	54.32	6.42	2.724	$8.46 \times 10^6$
S-F	-	5.61	3.321	-

of 3.58 to 13.04 cc/g) while the ratio of the surface area (in  $m^2/g$ ) to the pore volume (in  $m^3/g$ ) ranged from  $8.46 \times 10^6$  to  $1.90 \times 10^8 m^{-1}$ . On the other hand, the measured particle size from the different models showed a range of 1.923 (HK to 5.923 nm (S-F). Based on the range observed for the pore parameters of the nanoparticles from the different models, it is most likely that the synthesized material is a mesoporous nanoparticle. Porosity classification for mesoporous materials is in the range of 2 to 50 nm for mesoporous, 0.2 nm for microporous, and  $> 50$  to 100 nm for microporous. The significance of porosity in the determination of the effectiveness of nanomaterials in surface applications agrees with the trend that the lower the pore diameter and the higher the surface area, the better the expected performance. Based on the  $R^2$  values obtained for the different models, the M-BET and B-JH model. The evaluated M-BET surface area is lower than the value of 785 and 747  $m^2/g$  reported by Odiongenyi et al. [33] and Mostapha et al. [34] for CaO–NP obtained from bonnet shells and mud waste; they also reported pore

diameter in the mesoporous dimension. However, the measured particle size showed a significant improvement over average values of 6.17 and 77.4 m<sup>2</sup>/g, as reported by Khine *et al.* [35] and Jalu *et al.* [36], both for mesoporous CaO–NP. Another significant performance index for nanoparticles is the surface area to volume ratio which are related higher than those evaluated for the listed examples (Table 1).

The variation in the observed pore parameters of the synthesized CaO–NPs (compared to some reported works) can be related to alteration in some factors, such as the method of synthesis, source of raw materials, calcination temperature, and duration of calcination [37, 38]. The calculated dimension of the nanoparticles indicates that the CaO–NPs is under the mesoporous class of nanoparticles [39]. A similar dimension has been reported for CaO–NPs, which we synthesized from different oyster shells [40].

The scanning electron micrograph and the Fourier-transformed infrared (FT-IR) of the CaO–NPs are shown in Fig. 2. The micrograph reveals the dispersing of porous appearance in the internal structure of the CaO–NPs. On the other hand, the infrared absorption bands manifested at the following frequencies: 3642, 1407, and 872 cm<sup>-1</sup>. The narrow band at 3642 cm<sup>-1</sup> is due to OH stretching from the traces of H<sub>2</sub>O [41], while the peak at 1407 cm<sup>-1</sup> is typical for Ca–O vibration in the CaO–NPs [42].

The diffractogram obtained from the XRD analyses of the CaO–NPs is shown in Fig. 3a. The most intense peak was observed at [2Theta] = 34.2163° with an intensity

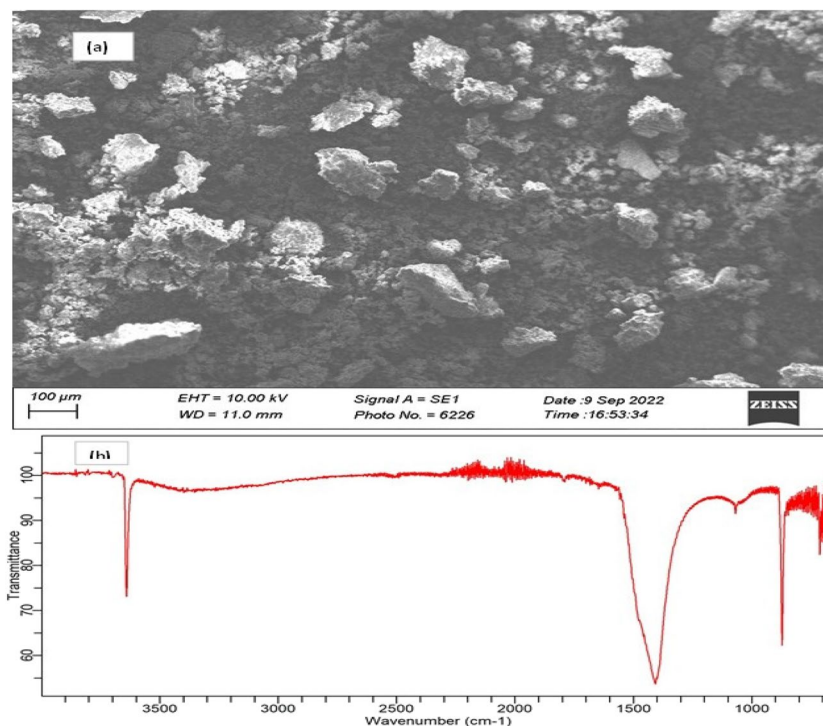
of 1706.24 cps while others were found at 18.1561, 29.4876, 47.1828, and 50.917°. The corresponding intensities were 1011.77, 1466.09, 694.78, and 50.92° respectively, and the full width at half maxima ( $\beta$ ) are shown in Table 2. Such reference peaks (especially at 34.2163°) have been observed for CaO–NPs by other researchers, thereby confirming that the synthesized materials are CO–NP [43–45]. The application of Scherrer's equation (Eq. 4) was useful in the determination of the size ( $d_x$ ) of the CaO–NPs crystallite [46, 47].

$$d_x = \frac{k\lambda}{\beta \cos\theta} \quad (4)$$

In the above equation,  $k$  and  $\lambda$  represent Scherrer's constant and the X-ray wavelength, respectively. The evaluated particle sizes for the various peaks are also shown in Table 2. Consequently, the average size of the crystallite is evaluated as 18.57 nm, which is comparable to results from works done on similar products using different precursors [48, 49].

The dislocation density for the nanoparticles was observed to range from 0.0524 to 0.0563 with an average value of 0.0539 nm<sup>-1</sup> (Table 1). The evaluated  $\delta$  values showed a decreasing trend with an increase in the diffraction angle (from 0.0563 to 0.0514 nm<sup>-1</sup>). However,  $d_x$  values tend to increase with an increase in the angle of diffraction from 17.77 to 19.44 nm (Table 1). Generally, the observed  $\delta$  values are relatively low, which suggests that the CaO–NP is relatively stable against deformation. The reported mean crystallite size also

**Fig. 2** a SEM micrograph. b FT-IR spectrum of CaO–NPs



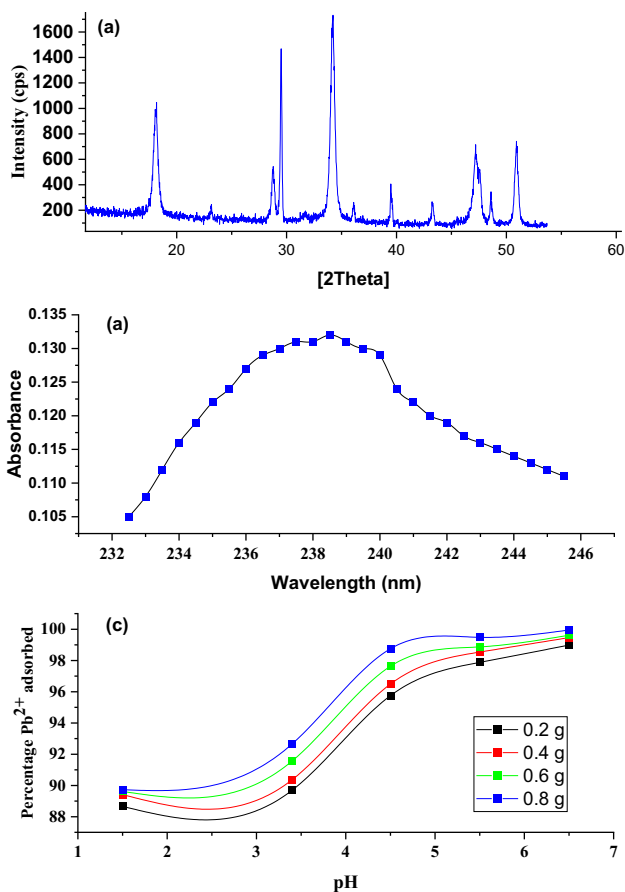


**Fig. 3** **a** XRD powder diffractogram. **b** Spectrum due to UV–visible absorption. **c** Variation of percentage adsorption with pH for CaO–NPs

confirms that the synthesized product has a nano dimension. The crystallite size can also be evaluated using the Williamson–Hall equation. This equation is based on the assumption that the total broadening is due to microstrain (i.e.  $\beta_{Micro} = 4\epsilon \tan\theta$ ) and crystallite size (defined as  $\beta_{Cryst} = \frac{k\lambda}{d_x \cos\theta}$ ). Therefore, the total broadening can be represented as,

$$\beta_{Total} = 4\epsilon \tan\theta + \frac{k\lambda}{d_x \cos\theta} \tag{5}$$

The rearrangement and simplification of Eq. 5 generated Eq. 6 as follows:

$$\beta_{Total} \cos\theta = 4\epsilon \sin\theta + \frac{k\lambda}{d_x} \tag{6}$$

The linearity of Eq. 6 for the tested CaO–NP was confirmed by an  $R^2$  value equal to 0.9776 while the crystalline, deduced from the intercept (i.e., 29.8 nm), showed some degree of agreement with the average value (18.574 nm) obtained from the Scherer equation. However, the slightly higher values obtained from the Williamson–Hall model are in agreement with most experimental findings that the Williamson–Hall model tends to overestimate crystallite size by over 35% [50].

In the crystal system, the interplanar distance is related to the Miller indices and the lattice constant of the CaO–NP according to Eq. 7.

$$\frac{1}{d_{hkl}^2} = \frac{h^2}{a^2} + \frac{k^2}{b^2} + \frac{l^2}{c^2} \tag{7}$$

Since CaO–NP is a cubic crystal,  $a=b=c$ . Therefore, Eq. 7 can be simplified to the following equations (Eqs. 8 and 9).

$$\frac{1}{d_{hkl}^2} = \frac{h^2 + k^2 + l^2}{a^2} \tag{8}$$

$$d_{hkl} = \frac{a}{(h^2 + k^2 + l^2)^{\frac{1}{2}}} \tag{9}$$

However, the Bragg equation relates the  $d_{hkl}$  with the diffraction angle according to Eq. 10, which is simplified to Eq. 11

$$n\lambda = d_{hkl} \sin\theta \tag{10}$$

$$d_{hkl} = \frac{n\lambda}{2\sin\theta} \tag{11}$$

For a first-order diffraction order,  $n=1$ , and Eqs. 9 and 11 were equated to obtain the lattice parameter for the synthesized CaO–NP as follows:

$$a = \frac{\lambda}{2\sin\theta} \times (h^2 + k^2 + l^2)^{\frac{1}{2}} \tag{12}$$

The miller indices were obtained from the JCPD database corresponding to the different angles of diffraction and  $\lambda = 1.5406 \text{ \AA}$ . Based on the above equations, the calculated

**Table 2** Crystalline properties of the CaO–NPs

[2Theta](°)	Intensity (cps)	(hkl)	$\beta$ (Rad)	$d_x$ (nm)	SSA	$\delta$	$d_{hkl}$	$a$ (Å)
18.16	1011.77	001	0.47296	17.77	98.15	0.0563	4.8811	4.8811
29.49	1466.09	100	0.47299	18.15	96.10	0.0551	3.0265	3.0265
34.22	1706.24	111	0.47199	18.36	95.00	0.0545	2.6182	4.5349
47.18	694.78	200	0.4687	19.15	91.08	0.0522	1.9248	3.8497
50.92	725.40	220	0.4723	19.44	89.72	0.0514	1.7919	5.0682

values of the lattice parameters (average = 4.2741 Å) and  $d_{hkl}$  (average = 2.8485 Å) are recorded in Table 2. The specific surface area of the CaO–NP was also calculated using the Sauter equation given as Eq. 13:

$$SSA = \frac{6000}{\rho d_x} \quad (13)$$

The symbol  $\rho$  in Eq. 13 defines the density of the CaO–NP, and its crystallite size is denoted by  $d_x$ . Based on the reported crystallite sizes, the evaluated SSA ranged from 89.72 to 98.15 m<sup>2</sup>/g, which is relatively higher than some literature values for CaO–NP, such as 77.4 m<sup>2</sup>/g reported by Jalu et al. [35] for CaO–NP obtained from egg shells. This suggests that with an enhanced specific surface area, the tendency towards photodegradation and adsorption is expected to be higher [51]. The evaluated surface area is lower than the value obtained from the BET method isotherm, which can be accounted for by the difference in the method of approach, explained by the consideration of pore diameter and crystallite size by the former and later methods, respectively.

However, the porosity of the nanoparticles based on the XRD density and the bulk density of the CaO–NP by applying Eq. 14.

$$Porosity = \left[ 1 - \frac{Bulkdensity}{X - raydensity} \right] \times \frac{100}{1} \quad (14)$$

The evaluated porosity is 59.74% and compares with the value of 47.84% deduced from the work of Jalu et al. [35] and therefore confirms that the synthesized CaO–NP is a mesoporous nanomaterial.

The spectrum arising from the absorption of UV by the CaO–NPs is shown in Fig. 3b. The spectrum reveals that the maximum wavelength ( $\lambda_{max(CaO-NPS)}$ ) of UV absorption by the nanoparticles is 239 nm, and therefore, we infer that the nanoparticles absorb in the UV range and have a characteristic band gap of 4.12 eV. This band gap ( $E_{BG(CaO-NPS)}$ ) was evaluated from the Planck equation (Eq. 5) [52],

$$E_{BG(CaO-NPS)} = h \times \frac{1}{\lambda_{max(CaO-NPS)}} \quad (15)$$

Other reported works have confirmed closely related  $\lambda_{max(CaO-NPS)}$  and  $E_{BG(CaO-NPS)}$  for CaO–NPs [52].

### 3.2 Variables influencing the adsorption of Pb<sup>2+</sup> by CaO–NPs

The pH for optimum absorption of the Pb<sup>2+</sup> was evaluated at around 6.4, as shown in Fig. 3c. The rise in adsorption became sharper above the pH of 3 and displayed an almost steady trend at pH close to 6. The adsorption removal

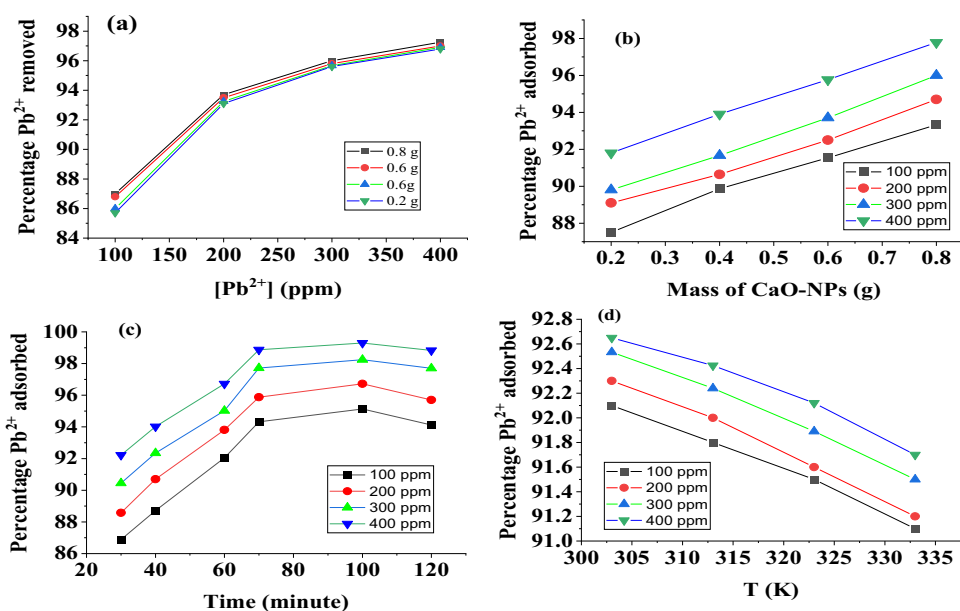
of the heavy metal ion progresses with increasing pH up to this optimum value. We could not continue the experiment beyond the pH of 6.4 to eliminate errors that could be introduced by precipitation. Such observations have been reported elsewhere with close pH values for the adsorption removal of Pb<sup>2+</sup> from aqueous solution [53–55]. The observed trend reveals that the adsorption of the positively charged Pb<sup>2+</sup> is favoured by alkaline pH, which is dominantly negative. At alkaline pH, the attraction of the metal ion is most likely because of the prevailing negatively charged surface. Still, at acidic pH, the surface can repel the lead ion such that as the population of positive charges increases, the uptake of Pb<sup>2+</sup> also increases. The observed pH for maximum adsorption is also consistent with reported values of the pH at the point of zero charge for CaO–NP but with irregularity after that optimum pH due to the changes in the mechanism from adsorption to precipitation [55, 56].

Figure 4 contains plots demonstrating the changes in the percentage lead (II) adsorbed under different experimental controlled conditions. Figure 4a shows that the magnitude of adsorption increases with an increase in the concentration of the heavy metal. The initial rise in the percentage of dye adsorbed with [Pb<sup>2+</sup>] was very sharp between [Pb<sup>2+</sup>] of 100 and 200 ppm corresponding to adsorption efficiency of 61 and 94%, respectively. However, above the [Pb<sup>2+</sup>], the efficiency progressively rises to about 98%. Lead ion adsorption can be significantly dependent on the number of available surface area. The large surface area and surface area to volume ration that characterized nanoparticles such as CaO–NP suggest that the adsorption will progress until all the available site is occupied.

A consideration of interplay between the mass of the adsorbent and the concentration of lead ion on adsorption indicated that although adsorption was higher at higher concentrations, similarities in the pattern became obvious irrespective of the mass of the adsorbent dosages (Fig. 4a), indicating that the mechanism of adsorption is independent on the concentration of the lead ions or the mass of the adsorbent. The observed increase in percentage adsorption with increasing initial Pb<sup>2+</sup> concentration also confirmed that the number of lead ions that are transported to the surface of the CaO–NPs increases as the concentration increases.

Adsorbent dosage can display a significant influence on the adsorption of lead ions through its influence on the number of available adsorption sites and available surface area. Based on the pattern of plots displayed in Fig. 4b, maximum adsorption approaching 100% was observed at a lead concentration of 400 ppm and adsorbent dosage of 0.8 g. This optimum value is almost equal to the optimum observed when lead ion was a major factor under consideration. A short fall of only 2 from 100% efficiency (at a lower concentration of Pb<sup>2+</sup>) is excellent and therefore

**Fig. 4** Variation of percentage  $\text{Pb}^{2+}$  adsorbed by CaO–NPs with initial concentration (a), adsorbent dosage (b), time (c), and temperature (d)



positioned the used CaO–NP as an excellent adsorbent for the removal of  $\text{Pb}^{2+}$ . A combination of the influence of the two factors showed an increase in the percentage removal of  $\text{Pb}^{2+}$ , tending to an optimum value of almost 100% within 70 min before a slight drop and steady trend. The observed trend for the variation of the amount of lead ions adsorbed with adsorbent dosage is consistent with some documented results concerning the adsorption of  $\text{Pb}^{2+}$  by watermelon waste [57], wall nutshell [58], where an increase in adsorption was also observed as the adsorbent dosage increase.

The use of CaO–NPs for separating  $\text{Pb}^{2+}$  from the aqueous solution also displayed better feasibility with time, as shown in Fig. 4c for various concentrations of  $\text{Pb}^{2+}$ . The effectiveness of time factors also became more favourable for higher concentrations of heavy metal ions. The drifting of the  $\text{Pb}^{2+}$  towards the CaO–NPs is a function of the time required for the  $\text{Pb}^{2+}$  to approach the adsorption sites and become equilibrated before the actual adsorption. Under the present study, The progress of adsorption, therefore, becomes more effective as the extent of interaction between the adsorbate and the adsorbent becomes enhanced with time and concentration. Higher concentrations of  $\text{Pb}^{2+}$  are also observed to show slight enhancement in adsorption, although the observed pattern of the plots for all concentrations follows a similar trend (Fig. 4c). A linear pattern between adsorption and period of contact was observed, and this corresponded to efficiency ranging from 83 to 99% within the first 70 min. After this, a further increase in time did not reflect a significant rise in adsorption. At a concentration of 100 to 400 ppm, the maximum adsorption ranged from about 93 to 99%, respectively. This also agrees with the role of adsorbate concentration in adsorption efficiency. When adsorption starts, it requires time to progress and two options are possible, namely,

a decrease in adsorption with time that maybe attributed to an increased rate of desorption or a limited number of active and vacant adsorption sites. On the contrary, the observed increase in adsorption with time shows that the tendency towards adsorption is higher than the tendency towards desorption and that the surface of the adsorbent was not significantly deactivated as the adsorption progressed. Published works showing similarity in trend for the variation of  $\text{Pb}^{2+}$  adsorption with time have been documented for some adsorbents [59, 60].

Any factor that can slow down the rate of migration of the lead ion from the bulk solution to the surface of the adsorbent can affect the extent of adsorption. Such factors may result in physical changes. However, the effect of temperature can become more severe on the adsorption of ions to the surface of the nanoparticles. We observed from Fig. 4d that between a temperature of 303 and 333 K, adsorption efficiency achieved a maximum decrease to 92, 91.6, 91.2, and 9.05% for  $[\text{Pb}^{2+}]$  corresponding to 100, 200, 300, and 400 ppm, respectively. The general trend shows a decrease in adsorption with an increase in temperature and confirms that the mechanism of adsorption is physical adsorption. This trend can be due to the deactivation of the adsorption surface, which may lead to an increase in desorption. We confirmed by some reported works that our observation has some support from some published works [61].

### 3.3 Kinetic of the adsorption

Although several kinetic models were tested for their fitness through linear plots and evaluated error values, the models that generated good fits for the adsorption of  $\text{Pb}^{2+}$  were pseudo 1st order (PDFO) [62], pseudo 2nd order (PDSO) [63], Elovich (EL) [64], Weber Morris (W–M) [65], and

Liquid film (L-F) [66] kinetics. Therefore, these models are hereby assessed in this sub-section. The linear forms of the listed models are represented by Eq. 6, 7, 8, 9 and 10), while the respective plots are shown in Fig. 5a–d respectively [67–70].

$$\ln(Q_e - Q_t) = \ln(Q_e) - k_{FO}t \quad (16)$$

$$\frac{t}{Q_t} = \frac{t}{Q_e} + \frac{1}{k_{SO}Q_e^2} \quad (17)$$

$$Q_t = \frac{1}{\beta} \ln(\alpha \beta) + \frac{1}{\beta} \ln(t) \quad (18)$$

$$Q_t = k_{M-W}t^{0.5} + C_{M-W} \quad (19)$$

$$-\ln\left(1 - \frac{Q_t}{Q_e}\right) = k_{L-F}t + C_{L-F} \quad (20)$$

Also, from the slopes and intercepts of the plots, data calculated for the various kinetic parameters are provided in Table 3. The mean square errors are also provided for the respective model [71] The PDSO presents higher values of  $R^2$  and lowers the error values (Fig. 5a and Table 3) than the PDFO model (Table 3). Therefore, the assumptions behind the PDSO can explain the adsorption of  $Pb^{2+}$  better than that of the PDFO. The PSFO model assumes that the

diffusion through the interface is a significant mechanism in the adsorption of the metal ion. Theoretical equilibrium adsorption capacity evaluated from the PSFO plots ranges from 244.29 to 613.99 mg/g and tends to increase with an increase in the concentration of  $Pb^{2+}$ . From 100 to 400 ppm. On the other hand,  $Q_e$  values obtained from the PDSO plots ranged from 104.09 to 104.49 mg/g and showed significant closeness with experimental values. The initial adsorption rate obtained from the  $Q_e$  values (*i.e.*  $k_2Q_e^2$ ) [76], ranged from 18.66 to 28.62 and tended to increase with an increase in the concentration of the lead ion. The PDFO rate constants for the different concentrations of the  $Pb^{2+}$  ranged from 0.0015 to 0.0084 /min, while those of PDSO showed a range of 0.001905 to 0.002622 /min. Both kinetic rate data showed an increasing trend as the concentration of the metal ion increased. This indicates that the adsorption is faster as the adsorbent dosages increase. Reported studies showing similarity in the fitness of PDFO kinetics concerning  $Pb^{2+}$  adsorption have been documented in the literature [72–74]. However, overwhelming literature supports the PDSO model. Based on the above analysis and the information presented in Table 3, the PDSO model offers a better description of the kinetics of the adsorption removal of the  $Pb^{2+}$  than the PDFO model because the PDSO presents higher values of  $R^2$  and lower values of the sum of squares as well as the mean square errors (Table 3). The applicability of the PDSO model suggests that the chemisorption mechanism tended to occur after the initial physical adsorption.

**Fig. 5** Kinetic plots for the adsorption of  $Pb^{2+}$  based on PSFO (a), Elovich (b), W-M diffusion (c), and T-L diffusion models (d)

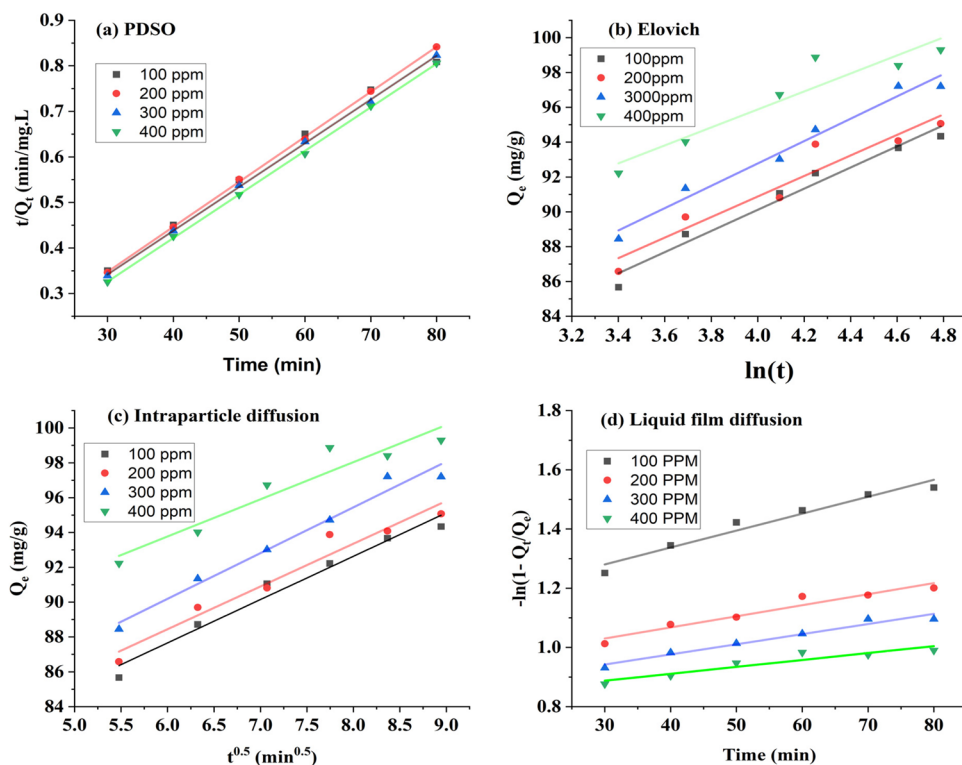




**Table 3** Kinetic parameter for the adsorption of Pb<sup>2+</sup> by CaO–NPs

Model/ parameter	100 ppm	200 ppm	300 ppm	400 ppm
<b>PDFO</b>				
R <sup>2</sup>	0.9956	0.9774	0.9797	0.9799
k <sub>FO</sub> (min <sup>-1</sup> )	0.0015	0.0029	0.0074	0.0083
Q <sub>e</sub> (mg.g <sup>-1</sup> )	244.29	342.92	470.91	613.99
SSE	4.37E-04	0.00123	1.69E-04	4.78E-05
MS	2.18E-04	6.27E-04	8.43E-05	2.34E-05
<b>PDSO</b>				
R <sup>2</sup>	1.0000	0.9998	0.9998	0.9998
Q <sub>e</sub> (mg.g <sup>-1</sup> )	101.2146	104.0583	104.1667	104.4932
k <sub>SO</sub> (min <sup>-1</sup> )	0.001905	0.001723	0.001723	0.002622
h	19.5122	18.65672	18.69159	28.62869
SSE	6.034E-05	2.34E-05	6.8096E-05	6.8606E-05
MSE	1.4086E-05	1.400R-05	2.4193E-05	1.5401E-05
<b>E-L</b>				
R <sup>2</sup>	0.9227	0.9745	0.9221	0.8987
β	0.1216	0.1558	0.1696	0.1928
α	383,691.90	15,320.50	5397.62	135.50
SSE	7.9331	1.5111	4.1089	4.2083
MSE	1.9808	1.0521	1.0272	1.0521
<b>W-M</b>				
R <sup>2</sup>	0.9708	0.9777	0.9163	0.9168
k <sub>W-M</sub>	2.4884	2.4554	2.6276	2.1332
Const	72.7246	73.7052	74.4201	80.9658
SSE	1.5574	2.3320	1.4640	3.4679
MSE	0.3894	0.7791	0.3505	0.8645
<b>L-F</b>				
R <sup>2</sup>	0.9965	0.9992	0.9796	0.9800
k <sub>L-F</sub>	0.0057	0.0038	0.0034	0.0023
SSE	0.0200	0.0019	7.693E-04	0.0012
MSE	6.2939E-04	3.9785E-04	1.9234E-04	3.036E-04

The EL plot is shown in Fig. 5b, and from a theoretical background, the EL is typical for the chemisorption mechanism [44]. However, sensing from the trends observed for the variation of the amount of Pb<sup>2+</sup> adsorbed with temperature, the initial adsorption mechanism for Pb<sup>2+</sup> is physical adsorption; therefore, chemisorption might have been a succeeding mechanism to the initial adsorption. However, the calculated sum of square (SSE) and mean square (MSE) errors are much larger than those observed for the PDSO. Relatively, lower R<sup>2</sup> values were also observed; suggesting that the Elovich model is not the most suitable model for the explanation of the kinetic of the adsorption of Pb<sup>2+</sup> by the synthesized CaO–NPs.

Diffusion of the metal ions from the bulk solution to the surface of the nanoparticles is a significant factor in the adsorption kinetics. Consequently, the major diffusion

models were tested, which are the L-F (Eq. 9) and M-W (Eq. 10) models. Based on the MSE, SSE, and is<sup>2</sup> values, lower errors, zero slopes, and better R<sup>2</sup> are predicted by the L-F model than the W-M model, which suggests that thin film diffusion dominates the adsorption kinetics. Similar diffusion models have been observed for the adsorption of lead (II) by some adsorbents such as biosorbents [75], metal–organic framework [76], and biowaste [77]. The rate constants evaluated from the L-F models are in good agreement with those associated with the PDSO. The model shows some dependency on the concentration of Pb<sup>2+</sup>, as shown by the observed variation in the diffusion constant and the liquid film boundary parameters (Table 3). This conclusion does not however rule out the influence of the intra-particle diffusion model completely, especially when considering the influence of concentration on the diffusion of the lead ion. The observation of the W-M boundary parameter showed an increased improvement with an increase in concentration but higher rate values compared to those reported for the L-F model (Table 3).

From the presented data (Table 3), the kinetic of the adsorption removal of Pb<sup>2+</sup> from aqueous solution is best described by the PDSO and L-F models because the two models present the least error values and higher R<sup>2</sup> values compared to other models.

### 3.4 Adsorption isotherms for Pb<sup>2+</sup>

Different adsorption models were tested for their applicability in the explanation of the adsorption characters of Pb<sup>2+</sup> unto the surface of CaO–NPs. Tested models were evaluated based on the R<sup>2</sup>, SSE, and MSE values, and those with R<sup>2</sup> > 0.9 were selected for further analysis. The models that met the listed conditions were the Freundlich (F-R), Temkin (T-N), Langmuir (L-N), Elovich (E-L), Dubinin-Raduskovich (D-R), and Halsey (H-S) isotherms. Expressions for the listed isotherms are shown in Eqs. 11 to 1, respectively. Figure 6 shows representative plots for the fitted models and parameters deduced from all the plots are recorded in Table 4 [78, 79].

$$\ln Q_e = \frac{1}{n} \ln C_e + \ln k_{F-R} \tag{21}$$

$$Q_e = B_{T-N} \ln C_e + B_{T-N} \ln k_{T-N} \tag{22}$$

$$\frac{C_e}{Q_e} = C_e \frac{1}{Q_{max}} + \frac{1}{Q_{max} k_{L-N}} \tag{23}$$

$$\ln \left( \frac{C_e}{Q_e} \right) = \ln (K_{E-L} Q_{max}) - \frac{Q_e}{Q_{max}} \tag{24}$$

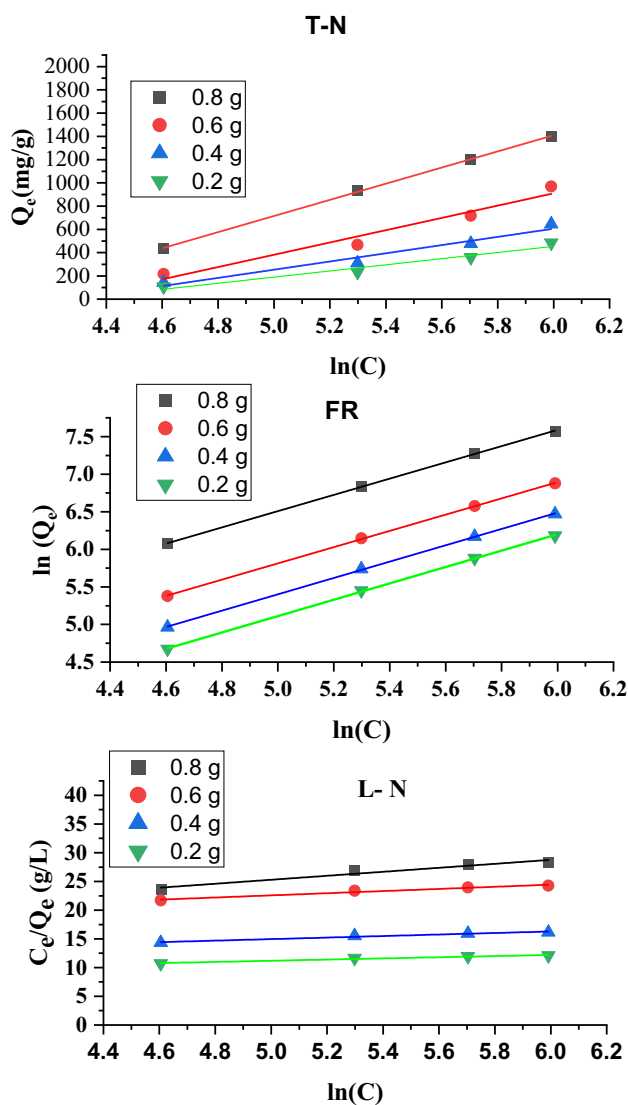


**Fig. 6** Representative isotherms for the adsorption of  $\text{Pb}^{2+}$  based on T-N, F-R, and L-N a equations

$$Q_e = -k_{D-R} \left[ RT \ln \left( 1 + \frac{1}{C_e} \right) \right]^2 + \ln Q_{max} \quad (25)$$

$$\ln Q_e = \frac{1}{n_{H-S}} (\ln k_{H-S}) - \frac{1}{n_{H-S}} \ln \left( \frac{1}{C_e} \right) \quad (26)$$

The Freundlich model (Eq. 11) explains the heterogenous adsorption project with the Freundlich constants ( $k_{F-R}$  and  $1/n_{F-R}$ ) representing the adsorption capacity and intensity of the adsorption, respectively [80]. Judging from the value of  $n_{F-R}$  adsorption can be predicted to be linear, cooperative, favourable, or unfavourable [81]. Also, the Langmuir isotherm (Eq. 13) has two major constants, namely, the Langmuir maximum adsorption capacity ( $Q_{max}$ ) and the

adsorption–desorption equilibrium constant ( $k_{L-N}$ ).  $Q_{max}$  values are informative in the provision of the reference point for the prediction of favourable adsorption based on the magnitude of the separation factor (calculated values not shown) and the intensity factor [82]

Since the F-R model gave better  $R^2$  values and lower errors than the Langmuir model. The tendency for the adsorption of  $\text{Pb}^{2+}$  largely included the multilayer process, which has also been observed for the adsorption of  $\text{Pb}^{2+}$  by other adsorbents [81]. The evaluated values of  $n_{F-R}$  are less than unity and show no significant difference for the various masses of the adsorbent. Literature concerning the  $n_{F-R}$  is in support of normal adsorption for  $\frac{1}{n_{F-R}} < 1$  while cooperative adsorption is feasible for  $\frac{1}{n_{F-R}} > 1$ . Also, the values of  $n_{F-R}$  within the range of 1 and 10 are consistent with favourable adsorption [83]. Based on the documented values of  $n_{F-R}$  calculated for the adsorption of  $\text{Pb}^{2+}$  by the nanoparticles (Table 4), it can be concluded that cooperative and favourable adsorption defined the adsorption characteristics of the adsorbate on the CaO–NPs.

The error values for the T-N model (Eq. 12) were relatively high compared to other models (Table 4), and the  $R^2$  values were comparable. Generally, the T-N isotherm is founded on the fundamental that the adsorption heat decreases as the surface coverage of the adsorbent increases [84]. Given the present results (Table 4), the values of the heat of adsorption for the various masses of the adsorbents are significantly low and technically support the involvement of physical adsorption, as observed in this study [85].

Although evaluated error values for the fitness of the D-R model were relatively high, the model displayed good  $R^2$  values and from the slope and intercept values of the plots, the D-R adsorption variables for the different masses of the CaO–NPs were obtained and recorded in Table 3. The essential significance of the model is that the adsorption energy was evaluated as the inverse of  $\sqrt{2k_{D-R}}$ . Consequently, the calculated adsorption energies, which ranged from 24.1 to 34.4 J/mol, are below the 16 kJ/mol threshold acceptable for the mechanism of chemical adsorption. Therefore, the operation of physc adsorption is confirmed. Such a report has been confirmed for the adsorption of  $\text{Pb}^{2+}$  onto rice bran surfaces [86].

The Elovich model also displayed excellent adsorption parameters based on the evaluated coefficient of determination and error functions, as shown in Table 4. The model is aligned with multilayer adsorption and is founded on the basis of exponential increment of adsorption site with adsorption [87]. The model also displayed a better prediction of maximum adsorption capacity compared to the prediction from the L-N model. The adsorption removal of  $\text{Pb}^{2+}$  has been reported elsewhere to be consistent with the Elovich isotherm, as observed in this work [88, 89].

**Table 4** Isotherm parameter for the adsorption of Pb<sup>2+</sup> by CaO-NPs

Model/parameter	0.8 g	0.6 g	0.4 g	0.2 g
<b>T-N</b>				
<i>R</i> <sup>2</sup>	0.904	0.9996	0.9797	0.9988
<i>B</i> <sub>T-N</sub>	694.34	225.91	470.79	113.24
Slope	69.54	225.91	470.79	113.24
SSE	5.03	3.11	5.52	3.09
MSE	11.35	7.58	2.76	1.55
<b>F-R</b>				
<i>R</i> <sup>2</sup>	0.9998	0.9998	0.9998	0.9997
<i>n</i> <sub>F-R</sub>	0.9246	0.9247	0.9196	0.9179
<i>k</i> <sub>F-R</sub>	0.7151	0.7368	1.5014	3.0132
Slope	1.0815	1.0814	1.0874	1.0894
Intercept	1.1013	0.4064	-0.0355	-0.3354
SSE	2.389 × 10 <sup>-4</sup>	2.482 × 10 <sup>-4</sup>	3.175 × 10 <sup>-4</sup>	3.405 × 10 <sup>-4</sup>
MSE	1.194 × 10 <sup>-4</sup>	1.24 × 10 <sup>-4</sup>	1.587 × 10 <sup>-4</sup>	1.703 × 10 <sup>-4</sup>
<b>L-N</b>				
<i>R</i> <sup>2</sup>	0.95042	0.9710	0.9680	0.9672
<i>Q</i> <sub>max</sub> (mg/g)	0.2880	0.5358	0.7516	0.9823
<i>k</i> <sub>L-N</sub>	0.434	0.1410	0.1601	0.1676
Slope	3.4683	1.83663	1.3305	1.0179
Intercept	7.9472	13.2412	8.3082	6.1035
SSE	6.803	3.090	3.811	3.811
MSE	3.402	1.540	1.906	1.906
<b>E-L</b>				
<i>R</i> <sup>2</sup>	0.9707	0.9650	0.9230	0.9599
<i>Q</i> <sub>max</sub> (mg/g)	909.09	478.47	313.47	238.10
<i>k</i> <sub>L-N</sub>	2.5737	2.420	2.3461	2.2729
Slope	0.0011	0.00209	0.00319	0.0042
Intercept	7.7578	7.0716	6.6005	6.2938
SSE	4.550 × 10 <sup>-2</sup>	4.971 × 10 <sup>-2</sup>	5.607 × 10 <sup>-2</sup>	5.945 × 10 <sup>-2</sup>
MSE	2.275 × 10 <sup>-2</sup>	2.485 × 10 <sup>-2</sup>	2.804 × 10 <sup>-2</sup>	2.972 × 10 <sup>-2</sup>
<b>H-S</b>				
<i>R</i> <sup>2</sup>	0.9051	0.9265	0.9278	0.9599
<i>n</i> <sub>H-S</sub>	0.1233	0.0716	0.0825	0.0825
<i>k</i> <sub>H-S</sub>	0.2859	0.1985	0.2139	0.2139
Slope	8.1071	13.9622	12.1154	12.1154
Intercept	-10.135	-22.5756	-18.6860	-18.6860
SSE	2.219 × 10 <sup>-1</sup>	2.327 × 10 <sup>-1</sup>	9.261 × 10 <sup>-2</sup>	9.261 × 10 <sup>-2</sup>
MSE	1.111 × 10 <sup>-1</sup>	1.116 × 10 <sup>-1</sup>	4.631 × 10 <sup>-2</sup>	4.631 × 10 <sup>-2</sup>

The Halsey isotherm also shows some degree of fitness based on the calculated *R*<sup>2</sup> and error values. The essential significance of this isotherm is that it is also applicable to multilayer adsorption processes involving porous material [90]. The fitness of the Halsey isotherm for the adsorption of Pb<sup>2+</sup> on silica-based adsorbent was confirmed by Chu et al. [91], and the reported Halsey adsorption parameters are relatively comparable to those obtained in this work. However, the adsorption parameters we have obtained from the slope and intercept of the plots do not

show significant differences at all levels of dosages of the nanoparticles (Table 4), suggesting that the isotherm may not be dosage-dependent concerning the nanoparticles. The error values were relatively minimal (i.e., within two decimal places), and the *R*<sup>2</sup> values for the plots extended from a minimum value of 0.9051 to 0.9599. The intensity parameters obtained from F-R (*n*<sub>F-R</sub>) and H-S (*n*<sub>H-S</sub>) isotherms are in good agreement and predict that the multilayer adsorption process increases with an increase in adsorbent dosage.

A close examination of the isotherm parameters presented in Table 4 indicates that the best-fitted isotherms are the F-R, H-S, and E-L isotherms because less error and excellent coefficient of determination are associated with these isotherms. Consequently, the formation of a multimolecular layer and mechanism of physical adsorption is proposed for the adsorption of  $\text{Pb}^{2+}$  by CaO-NPs.

### 3.5 Thermodynamics models for the adsorption of $\text{Pb}^{2+}$

The relationship between the standard free energy change of adsorption ( $\Delta G_{ads}^*$ ), enthalpy ( $\Delta S_{ads}^*$ ) and entropy ( $\Delta H_{ads}^*$ ) changes are given by the Gibb equation (Eq. 17) and are related to the adsorption equilibrium constant according to Eq. 18. The combination of the two equations led to Eq. 19 [92, 93].

$$\Delta G_{ads}^* = \Delta H_{ads}^* - T\Delta S_{ads}^* \quad (27)$$

$$\Delta G_{ads}^* = -RT \ln k_e = -RT \ln \left( \frac{C_0 - C_e}{C_e} \right) \quad (28)$$

$$\ln \left( \frac{C_0 - C_e}{C_e} \right) = \frac{\Delta S_{ads}^*}{R} - \frac{\Delta H_{ads}^*}{RT} \quad (29)$$

The thermodynamic significance of Eq. 19 is that the slope of the plot of  $\ln k_{ads}$  versus  $1/T$  (Fig. 7) is equal to the enthalpy change divided by the gas constant while the intercept is equal to the entropy change divided by the gas constant. Calculated thermodynamic variables are recorded in Table 5. The favouritism of the model expressed by Eq. 19 is strongly supported by the excellent values of  $R^2$  and the low values of SSE and MSE (Table 5). The listed enthalpy and entropy changes show a proportional dependency on the initial  $\text{Pb}^{2+}$  concentration. The adsorption is exothermic and displayed positive entropy changes, which may suggest less interaction between the adsorbate and the CaO-NPs and further confirm the operation of a physisorption mechanism.

### 3.6 Photoactivation of adsorption

The exposure of the batch adsorption experimental setup to a UV light source significantly enhances the adsorption capacity of the CaO-NPs for  $\text{Pb}^{2+}$ . This may be attributed to the activation of the adsorbent by UV radiation since the calculated band edge for the CaO-NPs (4.12 eV) suggests that it can absorb in this region. It can be confirmed from Fig. 8 that there is a significant enhancement in efficiency with an optimum value approaching almost 100% compared to about 98% observed in the absence of UV light. Therefore, the adsorption of Pb (II) by CaO-NPs is strongly favoured under UV light.

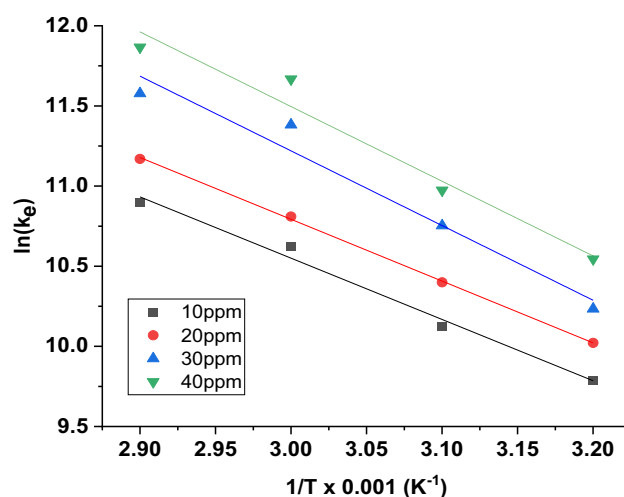


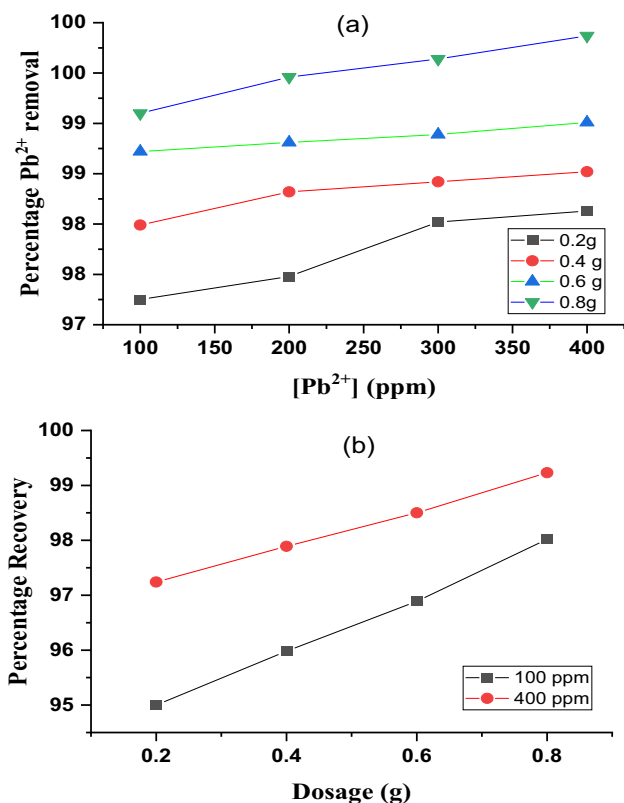
Fig. 7 Variation of  $\ln(k_e)$  with  $1/T$  based on the equation of the Transition state for  $\text{Pb}^{2+}$  adsorption unto CaO-NPs

Table 5 Thermodynamic adsorption variables for  $\text{Pb}^{2+}$  deduced from the plot of  $\ln k_{ads}$  against  $1/T$

Parameters	10 ppm	20 ppm	30 ppm	40 ppm
Slope	-3.8233	-3.8543	-4.6501	-4.6689
Intercept	22.0200	22.3560	25.2001	25.4730
$R^2$	0.9879	0.9792	0.9636	0.9942
$\Delta H_{ads} (J/mol)$	-31.7869	-32.0447	-38.6609	-38.8172
$\Delta S_{ads} (J/mol)$	183.0743	185.8678	209.5136	211.7825
SSE	0.0089	0.04107	0.01141	0.00043
MSE	0.00446	0.020153	0.0057	0.00022

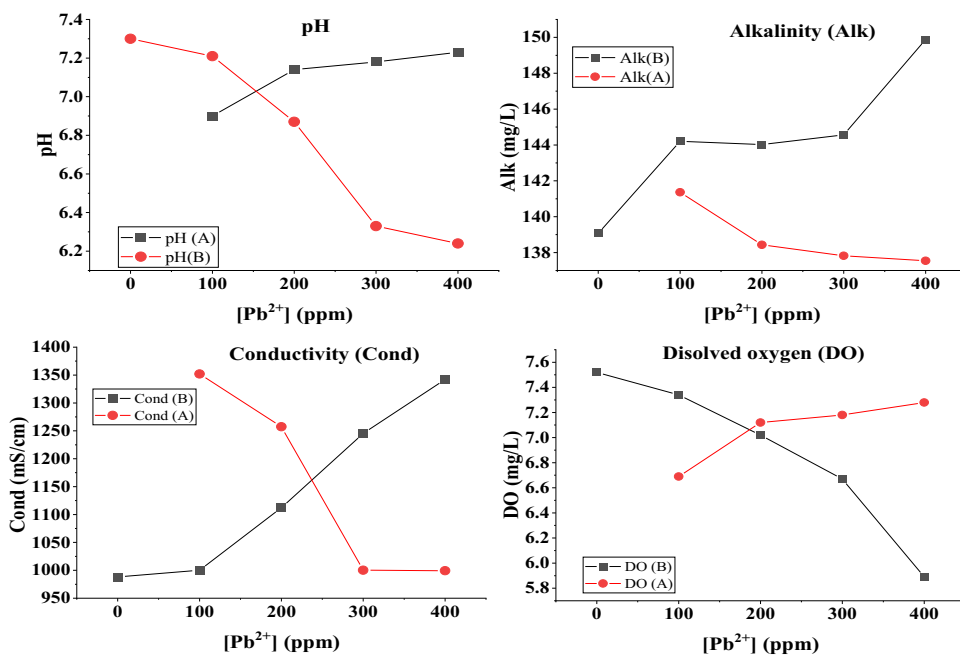
The reusability of the CaO-NPs was also investigated using different dosages of the used adsorbent for the re-trial experiment. The used adsorbent was washed severally with distilled water, dried, and reused. The results (Fig. 9b) indicated that at initial  $[\text{Pb}^{2+}]$  of 10 and 40 ppm, the adsorbent displayed efficiency above 98 and 99% respectively. The recovered adsorbent did not show any change in the major FT-IR peak at  $1400 \text{ cm}^{-1}$ , although there was a slight drop (by 0.7 units) in the intensity. This confirms that the adsorbent did not witness a significant denature after the first reuse. The concentrations of  $\text{Pb}^{2+}$  removed from the surface of the adsorbent were also re-determined, and the results reflected an almost 100% recovery when added to the equilibrium concentrations in the solution.

In Table 6, some literature data concerning the application of CaO-NPs as an adsorbent for  $\text{Pb}^{2+}$  are presented. From the recorded information, it is evident that most adsorption data favours the PDSO kinetics and that the present adsorbent has some levels of comparable advantages, especially when the photoactivated adsorption process is involved.



**Fig. 8** Variation of % Pb<sup>2+</sup> adsorbed with initial dye concentration after photoactivation (a) and % recovery of the adsorbent with dosage after reuse (b)

**Fig. 9** Variation of some physicochemical parameters (pH, Alk, Cond and DO) of water contaminated by different concentrations of lead (II) before (B) and after (A) adsorption



### 3.7 Changes in the physicochemical quality of the water

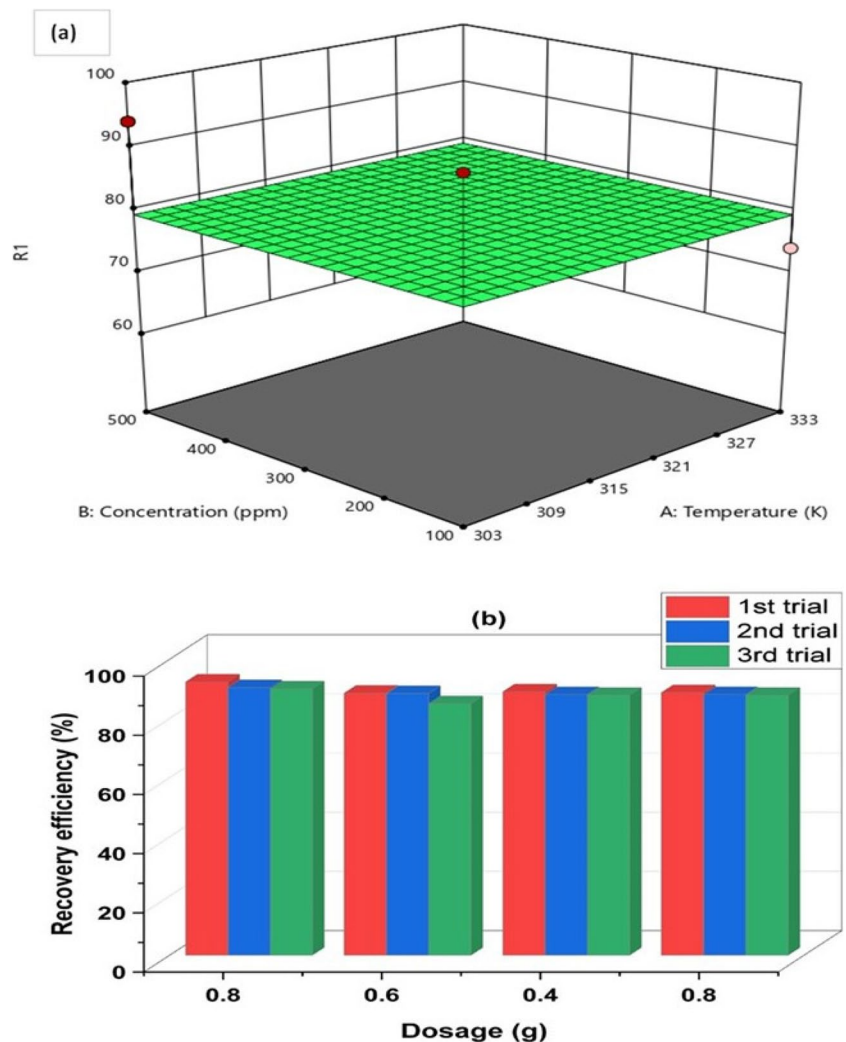
Measurements of some physicochemical parameters such as pH, conductivity, dissolved oxygen (DO), and alkalinity (alk) for the respective solution containing different concentrations of lead (II) ions were conducted before and after adsorption. The results obtained are shown in Fig. 9a–d. The initial addition of lead ions led to a decrease in pH (tending towards the acidic range) and DO. However, the pH (pH(A)) and DO (DO(A)) after adsorption removal of Pb(II) were favourably adjusted compared to their initial pH (PH(B) and DO (DO(B))). However, the alkalinity (Alk(B)) and conductivity (Cond(B)) showed an increment with the [Pb(II)] but were also readjusted after adsorption. Also adjusted after adsorption were the turbidity and salinity of the aqueous solution (plots not shown).

### 3.8 Optimization of the adsorption process/ interaction

The response surface analysis was used to optimize the adsorption process and to study the interaction between the associated variables. Figure 10a shows the response surface plots for the effect of concentration (A), temperature (B), adsorbent dosage (C), and time (D) on the adsorption removal of Pb<sup>2+</sup> from aqueous solution. The results obtained indicated that the highest interaction was contributed by temperature (42.67%), followed by time (26.22%), while adsorbent dosage showed 5.95% and concentration showed the least contribution (0.00197%). The interactions between the following factors concentration/temperature, concentration/dosage,

**Table 6** Literature values for the adsorption removal of  $Pb^{2+}$  by some nanoparticles

Nanoparticles	Removal efficiency (%)	Fitted isotherm	Fitted kinetics	References
CuONPs	87.00	Freundlich	Pseudo second order	[93]
MgSNPs	60.00	Freundlich	Pseudo second order	[94]
Dolomite-quartz $Fe_3O_4$ NPs	95.02	Langmuir	Pseudo second order	[95]
Nanomaghemite	60.00	-	Pseudo second order	[96]
CaO-NPs from eggshells	99.67	Langmuir	Oseido second order	[97]
CaO-NPs from eggshells	99.07	Langmuir	Pseudo second order	[55]
CaSiO <sub>3</sub> hydrogel	60.00	Langmuir	Pseudo second order	[98]
CaO-SiO <sub>3</sub> composites	99.58	Langmuir	Pseudo second order	[108]

**Fig. 10** Response surface analysis showing optimum conditions for the removal of lead ion by CaO-NPs (R1 = percentage  $Pb^{2+}$  removed)

concentration/temperature/dosage, concentration/dosage/time, temperature/dosage/time, and concentration/temperature/dosage/time showed the following percentage contributions, 0.23, 0.82, 6.06, 2.22, 4.09, 4.09, and 0.17% respectively. These results indicated that the highest interaction is between concentration, temperature, and dosage, contributing

6.06%, while the least is between the four factors (0.17%) respectively. Based on the response surface analysis and the consideration of the four factors, optimum percentage removal approaching 70% can be achieved under the following conditions: concentration = 250 ppm, temperature = 318 K, adsorbent dosage = 0.5 g, and contact time = 75 min.

### 3.9 Recyclability of the adsorbent

The used adsorbents were washed thoroughly with distilled water, dried, and recalced for further application in the removal of the CaO–NPs. The results obtained after three trial experiments are shown in Fig. 10b. The Figure reveals that after three trials, the adsorbent could still retain more than 88% of its capacity, although a slight drop in efficiency was observed for every successive trial experiment.

## 4 Conclusion

CaO–NPs have been successfully synthesized, characterized, and applied for the removal of lead (II) ions from an aqueous solution. The CaO–NPs is a mesoporous material with an average crystalline size of 18 nm and shows a significant FT-IR peak due to Ca–O vibration. The adsorbent absorbs maximally in the UV region and displays a zeta potential that favours alkaline conditions for optimum removal of lead (II) ions from an aqueous solution. Other optimum conditions were a rise in the initial heavy metal ion concentration, dosages of the adsorbent, and a decline in temperature. A physical adsorption mechanism is operational for this system and is controlled by liquid film diffusion from the bulk solution to the CaO–NP surface through the interface. The adsorbent surface shows a stronger degree of heterogeneity rather than the homogenous counterpart. The CaO–NPs has functional stability and re-usability and favourably adjusted the quality of the water concerning conductivity, pH, dissolved oxygen, and alkalinity.

**Author contribution** The research was conceived by Nnabuk Okon Eddy, Richard Alexis Ukpe, and Paul Ocheje Ameh. The characterization study was done by Nnabuk Okon Eddy, Rajni Garg, Rishav Garg, Saikh Mohammad Wabaidur, Masoom Raza Siddiqui, and Raphael Ogbodo. Musa Runde and Iliya Dimas Kwanchi carried out the adsorption study. All authors wrote the first draft, revised, and edited the final manuscript.

**Funding** The research work that generated this publication was sponsored by the Tertiary Education Trust Fund of Nigeria (TETFUND) through the National Research grant (2020) with Prof. Nnabuk Okon Eddy as the Principal investigator (Grant number: TRTF/ES/DR&D-CE/NRF2020/SETI/98/VOL.1). The work was also supported by the Project Number (RSP2024R448), King Saud University, Riyadh, Saudi Arabia.

**Data availability** The datasets used or analyzed during the current study are available from the corresponding author upon reasonable request.

## Declarations

**Ethical approval and consent to participate** All authors approve the ethics and consent to participate in this research.

**Consent to publish** All authors have consented to publish this paper.

**Competing interests** The authors declare no competing interests.

## References

1. Aziz KHH, Mustafa E, Omer KM, Hama S, Hamarwi RF, Rahman KO (2023) Heavy metal pollution in the aquatic environment: efficient and low-cost removal approaches to eliminate their toxicity: a review. *RSC Adv* 13(26):17595–17610. <https://doi.org/10.1039/D3RA00723E>
2. Suami RB, Sivalingam P, Al Salah DM, Grandjean D, Mulaji CK, Mpiana PT, Breider F, Otamonga JP, Poté J (2020) Heavy metals and persistent organic pollutants contamination in river, estuary, and marine sediments from Atlantic Coast of Democratic Republic of the Congo. *Environ Sci Pollut Res Int* 27(16):20000–20013. <https://doi.org/10.1007/s11356-020-08179-4>
3. Nnaji ND, Onyeaka H, Miri T et al (2023) Bioaccumulation for heavy metal removal: a review. *SN Appl Sci* 5:125. <https://doi.org/10.1007/s42452-023-05351-6>
4. Ungureanu N, Vlăduț V, Voicu G (2023) Water scarcity and wastewater reuse in crop irrigation. *Sustainability* 2020(12):9055. <https://doi.org/10.3390/su12219055>
5. Akhtar S, Khan ZT, Ahmad K, Nadeem M, Ejaz A, Hussain MI, Ashraf MA (2022) Assessment of lead toxicity in diverse irrigation regimes and potential health implications of agriculturally grown crops in pakistan. *Agric Water Manag* 271(1):107743. <https://doi.org/10.1016/j.agwat.2022.107743>
6. Kumar VS, Pradhan JK, Sharma SK, Singh P, Sharma JK (2021) Structural, optical and antibacterial response of cao nanoparticles synthesized via direct precipitation technique. *Nano Biomed Eng* 13(2):172–178. <https://doi.org/10.5101/nbe.v13i2.p172-178>
7. Lehigh University (2022) Study confirms lead-in-water causes adverse fetal health outcomes. *ScienceDaily*. [www.sciencedaily.com/releases/2022/07/220713114629.htm](http://www.sciencedaily.com/releases/2022/07/220713114629.htm)
8. Narayana PL, Maurya AK, Wang X, Harsha MR, Srikanth O, Alnuaim AA, Hatamleh WA, Hatamleh AA, Cho KK, Paturi UMR, Reddy BS (2021) Artificial neural networks modeling for lead removal from aqueous solutions using iron oxide nanocomposites from bio-waste mass. *Environ Res* 199:111370. <https://doi.org/10.1016/j.envres.2021.111370>
9. Qasem NAA, Mohammed RH, Lawal DU (2021) Removal of heavy metal ions from wastewater: a comprehensive and critical review. *Npj Clean Water* 4:36. <https://doi.org/10.1038/s41545-021-00127-0>
10. Ahmed SF, Mofijur M, Parisa TA, Islam N, Kusumo F, Inayat A, Le VG, Badruddin IA, Khan TMY, Ong HC (2022) Progress and challenges of contaminate removal from wastewater using microalgae biomass. *Chemosphere* 286(Pt 1):131656. <https://doi.org/10.1016/j.chemosphere.2021.131656>
11. Shi L, Wang N, Hu X, Yin D, Wu C, Liang H, Cao W, Cao H (2023) Acute toxic effects of lead (Pb<sup>2+</sup>) exposure to rare minnow (*Gobiocypris rarus*) revealed by histopathological examination and transcriptome analysis. *Environ Toxicol Pharmacol* 79. <https://doi.org/10.1016/j.etap.2020.103385>
12. Eddy NO, Garg R, Garg R, Ukpe RA, Abugu H (2024) Adsorption and photodegradation of organic contaminants by

- silver nanoparticles: isotherms, kinetics, and computational analysis. *Environ Monit Assess* 196:65. <https://doi.org/10.1007/s10661-023-12194-6>
13. Maftouh A, El Fatni O, El Hajjaji S, Jawish MW, Sillanpää M (2023) Comparative review of different adsorption techniques used in heavy metals removal in water. *Biointerface Res App Chem* 13(4):397
  14. Chowdhury IR, Chowdhury S, Mazumder MAJ, Al-Ahmed A (2022) Removal of lead ions (Pb<sup>2+</sup>) from water and wastewater: a review on the low-cost adsorbents. *Appl Water Sci* 12(8):185. <https://doi.org/10.1007/s13201-022-01703-6>
  15. Ngamsurach P, Namwongsa N, Praipipat P (2022) Synthesis of powdered and beaded chitosan materials modified with ZnO for removing lead (II) ions. *Sci Rep* 12:17184. <https://doi.org/10.1038/s41598-022-22182-4>
  16. Ahmad K, Shah HR, Khan MS, Iqbal A, Potrich E, Amaral LS, Rasheed S, Nawaz H, Ayub A, Naseem K, Muhammad A, Yaqoob MR, Ashfaq M (2022) Lead In drinking water: Adsorption method and role of zeolitic imidazolate frameworks for its remediation: A review. *J Cleaner Prod* 368. <https://doi.org/10.1016/j.jclepro.2022.133010>
  17. Garg R, Garg R, Eddy NO, Almohana AI, Fahad S, Khan MA, Hong SH (2022) Biosynthesized silica-based zinc oxide nanocomposites for the sequestration of heavy metal ions from aqueous solutions. *J King Saud University-Sci.* <https://doi.org/10.1016/j.jksus.2022.101996>
  18. Mohanapriya V, Saktivel R, Pham NDK, Cheng CK, Le HS, Dong TMH (2023) Nanotechnology- A ray of hope for heavy metals removal. *Chemosphere* 311(Pt 1):136989. <https://doi.org/10.1016/j.chemosphere.2022.136989>
  19. Baby R, Hussein MZ, Abdullah AH, Zainal Z (2022) Nanomaterials for the treatment of heavy metal contaminated water. *Polymers* 14:583. <https://doi.org/10.3390/polym14030583>
  20. Eddy NO, Ukpe RA, Garg R, Garg R, Odionenyi AO, Ameh P, Akpet I, N. (2024) Enhancing water purification efficiency through adsorption and photocatalysis: models, application and challenges. *Int J Environ Anal Chem.* <https://doi.org/10.1080/03067319.2023.2295934>
  21. Motlswa MG, Badmus KO, Khotseng L (2022) Development of adsorptive materials for selective removal of toxic metals in wastewater: a review. *Catalysts* 12:1057. <https://doi.org/10.3390/catal12091057>
  22. Essien UI, Odionenyi AO, Obadimu CO, Obdimu IS (2023) Investigation of snail shells as an adsorbent and precursor for the synthesis of calcium oxide nanoparticles for the removal of amoxicillin from aqueous solution. *Comm Physical Sci* 8(4):453–464
  23. Eddy NO, Garg R, Garg R, Eze SI, Ogoko EC, Kelle HI, Ukpe RA, Ogbodo R, Chijoke, F (2023) Sol-gel synthesis, computational chemistry, and applications of CaO nanoparticles for the remediation of methyl orange contaminated water. *Adv Nano Res* 15(1):35–48. <https://doi.org/10.12989/anr.2023.15.1.000>
  24. Eddy NO, Odionenyi AO, Garg R, Ukpe RA, Garg R, El Nemir A, Ngwu CM, Okop IJ (2023) Quantum and experimental investigation of the application of *Crassostrea gasar* (mangrove oyster) shell-based CaO nanoparticles as adsorbent and photocatalyst for the removal of procaine penicillin from aqueous solution. *Environ Sci Pollut Res.* 30(23):64036–64057. <https://doi.org/10.1007/s11356-023-26868-8>
  25. Ogoko EC, Kelle HI, Akintola O, Eddy NO (2023) Experimental and theoretical investigation of *Crassostrea gigas* (gigas) shells based CaO nanoparticles as a photocatalyst for the degradation of bromocresol green dye (BCGD) in an aqueous solution. *Biomass Conversion and Biorefinery.* <https://doi.org/10.1007/s13399-023-03742-8>
  26. Kelle HI, Ogoko EC, Akintola O, Eddy NO (2023) Quantum and experimental studies on the adsorption efficiency of oyster shell-based CaO nanoparticles (CaONPO) towards the removal of methylene blue dye (MBD) from aqueous solution. *J Biomass Convers Biorefinery.* <https://doi.org/10.1007/s13399-023-04947-7>
  27. Bayuseno AP, Prasetya AI, Ismail R, Setiyana B, Jamari J (2022) Reuse of waste crab shells for synthesis of calcium carbonate as a candidate biomaterial. *Rasayan J Chem* 15(1):523–528. <https://doi.org/10.31788/RJC.2022.1516640>
  28. Ismail R, Cionita T, Shing WL, Fitriyana DF, Siregar JP, Bayuseno AP, Nugraha FW, Muhamadin RC, Junid R, Endot NA (2022) Synthesis and characterization of calcium carbonate obtained from green mussel and crab shells as a biomaterials candidate. *Materials* 15:5712. <https://doi.org/10.3390/ma15165712>
  29. Alghamdi AA, Al-Odayni A-B, Saeed WS, Al-Kahtani A, Alharthi FA, Aouak T (2019) Efficient adsorption of lead (II) from aqueous phase solutions using polypyrrole-based activated carbon. *Materials* 12:2020. <https://doi.org/10.3390/ma12122020>
  30. Oyekanmi AA, Latiff AAA, Daud Z, Mohamed RMSR, Ismail N, Aziz A, Rafatullah M, Hossain K, Ahmad A, Abiodun AK (2019) Adsorption of cadmium and lead from palm oil mill effluent using bone-composite: optimisation and isotherm studies. *Int J Environ Anal Chem* 99(8):707–725. <https://doi.org/10.1080/03067319.2019.1607318>
  31. Abdelatif Y, Gaber A.-AM, Fouda AE-AS, Alsoukary T (2020) Evaluation of calcium oxide nanoparticles from industrial waste on the performance of hardened cement pastes: physicochemical study. *Processes* 8:401. <https://doi.org/10.3390/pr8040401>
  32. Sinha P, Datar A, Jeong C, Deng X, Chung YG, Lin L (2019) Surface area determination of porous materials using the Brunauer–Emmett–Teller (BET) method: limitations and improvements. *The J Physical Chem C* 123(33):20195–20209. <https://doi.org/10.1021/acs.jpcc.9b02116>
  33. Odionenyi AO, Essien UI, Ukpong EJ, Ekwere IO (2023) Adsorption Efficiency of scotch bonnet shells as a precursor for calcium oxide nanoparticles and an adsorbent for the removal of amoxicillin from aqueous solution. *Communication in Physical Science* 9(3):367–382
  34. Mostafa FA, Gad AN, Gaber AAM et al (2023) Preparation, Characterization and application of calcium oxide nanoparticles from waste carbonation mud in clarification of raw sugar melt. *Sugar Tech* 25:331–338. <https://doi.org/10.1007/s12355-022-01150-2>
  35. Jalu RG, Ayala T, Kasirajan R (2021) Calcium oxide nanoparticles synthesis from hen eggshells for removal of lead (Pb(II)) from aqueous solution. *Environ Chem* 4(25):100193. <https://doi.org/10.1016/j.envc.2021.100193>
  36. Phromma S, Wutikhun T, Kasamechonchung P, Eksangri T, Sapharoenkun C (2020) Effect of calcination temperature on photocatalytic activity of Synthesized TiO<sub>2</sub> nanoparticles via wet ball milling sol-gel method. *Appl Sci* 10:993. <https://doi.org/10.3390/app10030993>
  37. Triphati A, Pirzadah TB (2023) Chapter 3 - Synthesis methods of nanoparticles and their key applications, Editor(s): Munir Ozturk, Arpita Roy, Rouf Ahmad Bhat, Fazilet Vardar-Sukan, Fernanda Maria Policarpo Tonelli, In *Micro and Nano Technologies. Synth Bionanomaterials Biomed Appl Elsevier* 57–76. <https://doi.org/10.1016/B978-0-323-91195-5.00001-5>.
  38. Eddy NO, Garg R, Garg R, Aikoye A, Ita BI (2022) Waste to resource recovery: mesoporous adsorbent from orange peel for the removal of trypan blue dye from aqueous solution. *Biomass Convers Biorefinery* 13:13493–13511. <https://doi.org/10.1007/s13399-022-02571-5>
  39. Eddy NO, Ukpe RA, Ameh P, Ogbodo R, Garg R, Garg R (2022) Theoretical and experimental studies on photocatalytic removal of methylene blue (MetB) from aqueous solution using oyster shell synthesized CaO nanoparticles (CaONP-O). *Environ Sci Pollut Res* 0(34):81417–81432. <https://doi.org/10.1007/s11356-022-22747-w>



40. Naik TSSK, Singh S, Narasimhappa P et al (2023) Green and sustainable synthesis of CaO nanoparticles: its solicitation as a sensor material and electrochemical detection of urea. *Sci Rep* 13:19995. <https://doi.org/10.1038/s41598-023-46728-2>
41. Nayeem A, Mizi F, Ali MF, Shariffuddin JH (2022) Utilization of cockle shell powder as an adsorbent to remove phosphorus-containing wastewater. *Environ Res.* 2023 Jan 1;216(Pt 2):114514. <https://doi.org/10.1016/j.envres.2022.114514>
42. Habte L, Shiferaw N, Mulatu D, Thenepalli T, Chilakala R, Ahn JW (2019) Synthesis of nano-calcium oxide from waste eggshell by sol-gel Method. *Sustainability* 11:3196. <https://doi.org/10.3390/su11113196>
43. Mushtaq M, Hassan SM, Mughal SS (2022) Synthesis, characterization and biological approach of nano oxides of calcium by *Piper nigrum*. *Am J Chem Eng* 10(4):79–88
44. Al-Odayni A-B, Alsubaie FS, Abdu NAY, Al-Kahtani HMAND, Saeed WS (2023) Adsorption kinetics of methyl orange from model polluted water onto N-doped activated carbons prepared from N-containing Polymers. *Polymers* 15:1983. <https://doi.org/10.3390/polym15091983>
45. Atchudan R, Perumal S, Joo J, Lee YR (2022) Synthesis and characterization of monodispersed spherical calcium oxide and calcium carbonate nanoparticles via simple pyrolysis. *Nanomaterials* 12:2424. <https://doi.org/10.3390/nano12142424>
46. Bold B-E, Urnuksaikhani E, Mishig-Ochir T (2022) Biosynthesis of silver nanoparticles with antibacterial, antioxidant, anti-inflammatory properties and their burn wound healing efficacy. *Front Chem* 10:972534. <https://doi.org/10.3389/fchem.2022.972534>
47. Jadhav VR, Bhagare AM, Lokhande DD, Vaidya C, Dhayagude A, Khalid M, Aher J, Mezni A, Dutta M (2022) Green synthesized calcium oxide nanoparticles (CaO NPs) using leaves aqueous extract of *Moringa oleifera* and evaluation of their antibacterial activities. *J Nanomater* 2:1–7. <https://doi.org/10.1155/2022/9047507>
48. Kumar A, Kumar A, M.M.S, C.-P., Chaturvedi AK, Shabnam AA, Subrahmanyam G, Mondal R, Gupta DK, Malyan SK, Kumar SS, A Khan, S, Yadav KK (2020) Lead toxicity: health hazards, influence on food chain, and sustainable remediation approaches. *Int. J. Environ. Res. Public Health*, 17, 2179 <https://doi.org/10.3390/ijerph17072179>
49. Maswanganye MW, Kabongo GL, Mathevela LE et al (2023) Unveiling the effect of strain engineering on the electrochemical properties of hydrothermally grown nanostructured indium doped ZnSeO<sub>3</sub> for photoanode applications. *Sci Rep* 13:20131. <https://doi.org/10.1038/s41598-023-47436-7>
50. Ayesha HI, Haider A, Shahzadi I, Moeen S, Ul-Hamid A, Nabgan W, Shahzadi A, Alshahrani T & Ikram H (2023) Polyvinylpyrrolidone and chitosan-coated magnetite (Fe<sub>3</sub>O<sub>4</sub>) nanoparticles for catalytic and antimicrobial activity with molecular docking analysis. *J Environ Chem Eng* 11(3). <https://doi.org/10.1016/j.jece.2023.110088>
51. Dompheh KA, Arthur DS, Mensah SY, Adu KM, Edziah R, Amejepewu M (2023) Effect of band-gap tuning on absorption of phonons and acoustoelectric current in graphene nanoribbon. *Physica E* 147:115516. <https://doi.org/10.1016/j.physe.2022.115516>
52. Gandhi N, Shruthi Y, Sinsha G, Anusha CR (2021) Facile and eco-friendly method for synthesis of calcium oxide (CaO) nanoparticles and its potential application in agriculture. *Haya The Saudi J Life Sci* 6(5):89–103. <https://doi.org/10.36348/sjls.2021.v06i05.003>
53. Thakur S, Singh S, Pal B (2021) Superior adsorption removal of dye and high catalytic activity for transesterification reaction displayed by crystalline CaO nanocubes extracted from mollusc shells. *Fuel Process Technol* 213. <https://doi.org/10.1016/j.fuproc.2020.106707>
54. de Menezes LB, Muraro PCL, Druzian DM, Ruiz YPM, Galembeck A, Pavoski G, Espinosa DCR, da Silva WL (2024) Calcium oxide nanoparticles: biosynthesis, characterization and photocatalytic activity for application in yellow tartrazine dye removal. *J Photochem Photobiol A Chem* 447. <https://doi.org/10.1016/j.jphotochem.2023.115182>
55. Kasirajan R, Bekele A, Girma E (2022) Adsorption of lead (Pb-II) using CaO-NPs synthesized by solgel process from hen eggshell: response surface methodology for modeling, optimization and kinetic studies. *S Afr J Chem Eng* 40:209–229. <https://doi.org/10.1016/j.sajce.2022.03.008>
56. Adebowale K, Egbedina A, Shonde B (2020) Adsorption of lead ions on magnetically separable Fe<sub>3</sub>O<sub>4</sub> watermelon composite. *Appl Water Sci* 10:225. <https://doi.org/10.1007/s13201-020-01307-y>
57. Alsohaimi IH, Nassar AM, Elnasr TA, S Cheba BA (2020) A novel composite silver nanoparticles loaded calcium oxide stemming from egg shell recycling: a potent photocatalytic and antibacterial activities. *J Cleaner Prod* 248. <https://doi.org/10.1016/j.jclepro.2019.119274>
58. Dehghani MH, Afsari Sardari S, Afsharnia M et al (2023) Removal of toxic lead from aqueous solution using a low-cost adsorbent. *Sci Rep* 13:3278. <https://doi.org/10.1038/s41598-023-29674-x>
59. Tejada-Tovar C, Villabona-Ortiz A, González-Delgado AD (2023) High-efficiency removal of lead and nickel using four inert dry biomasses: insights into the adsorption mechanisms. *Materials* 16:4884. <https://doi.org/10.3390/ma16134884>
60. Odoemelam SA, Emeh NU, Eddy NO (2018) Experimental and computational Chemistry studies on the removal of methylene blue and malachite green dyes from aqueous solution by neem (*Azadirachta indica*) leaves. *Journal of Taibah University of Science* 12(3):255–265. <https://doi.org/10.1080/16583655.2018.1465725>
61. Revellame ED, Fortela DL, Sharp W, Hernandez R, Zappi ME (2020) Adsorption kinetic modeling using pseudo-first order and pseudo-second order rate laws: a review. *J Cleaner Eng Technol* 1. <https://doi.org/10.1016/j.clet.2020.100032>
62. Kostoglou M, Karapantsios TD (2022) Why is the linearized form of pseudo-second order adsorption kinetic model so successful in fitting batch adsorption experimental data? *Colloids Interfaces* 6:55. <https://doi.org/10.3390/colloids6040055>
63. Edet UA, Ifeuebuegu AO (2020) Kinetics, isotherms, and thermodynamic modeling of the adsorption of phosphates from model wastewater using recycled brick waste. *Processes* 8:665. <https://doi.org/10.3390/pr8060665>
64. Wang J, Guo X (2022) Rethinking of the intraparticle diffusion adsorption kinetics model: interpretation, solving methods and applications. *Chemosphere* 309(2):136732. <https://doi.org/10.1016/j.chemosphere.2022.136732>
65. Hasani N, Selimi T, Mele A, Thaçi V, Halili J, Berisha A, Sadiku M (2022) Theoretical, Equilibrium, kinetics and thermodynamic investigations of methylene blue adsorption onto lignite coal. *Molecules* 2022(27):1856. <https://doi.org/10.3390/molecules27061856>
66. Varela, JP. (2023). On validity, physical meaning, mechanism insights and regression of adsorption kinetic models. *J Mol Liq* 376. <https://doi.org/10.1016/j.molliq.2023.121416>
67. Tran HN (2023) Applying linear forms of pseudo-second-order kinetic model for feasibly identifying errors in the initial periods of time-dependent adsorption datasets. *Water* 15:1231. <https://doi.org/10.3390/w15061231>
68. Robati D (2023) Pseudo-second-order kinetic equations for modeling adsorption systems for removal of lead ions using multi-walled carbon nanotube. *J Nanostruct Chem* 3:55. <https://doi.org/10.1186/2193-8865-3-55>
69. Taraba B, Bulavová P (2022) Second or pseudo-second-order model for adsorption kinetics? *Sep Sci Technol* 57(10):1558–1562. <https://doi.org/10.1080/01496395.2021.1998124>
70. Zand AD, Abyaneh MR (2020) Adsorption of Lead, manganese, and copper onto biochar in landfill leachate: implication of

- non-linear regression analysis. *Sustain Environ Res* 30:18. <https://doi.org/10.1186/s42834-020-00061-9>
71. Soldatkina L, Yanar M (2021) Equilibrium, kinetic, and thermodynamic studies of cationic dyes adsorption on corn stalks modified by citric acid. *Colloids Interfaces* 1(5):52. <https://doi.org/10.3390/colloids5040052>
  72. Jayakumar S, Sudarsan S, Sridhar B, Parthiban F, Prabu AV, Jha S (2023) Synthesis, characterization, and performance of chitosan/nylon 6/polyurethane blend for the removal of chromium (VI) and lead (II) ions from aqueous solutions for enhanced kinetic adsorption studies. *Water Reuse* 13(3):319–328. <https://doi.org/10.2166/wrd.2023.019>
  73. Manjuladevi M, Anitha R, Manonmani S (2018) Kinetic study on adsorption of Cr(VI), Ni(II), Cd(II) and Pb(II) ions from aqueous solutions using activated carbon prepared from *Cucumis melo* peel. *Appl Water Sci* 8:36. <https://doi.org/10.1007/s13201-018-0674-1>
  74. Ton-That L, Huynh TNL, Duong BN et al (2023) Kinetic studies of the removal of methylene blue from aqueous solution by biochar derived from jackfruit peel. *Environ Monit Assess* 195:1266. <https://doi.org/10.1007/s10661-023-11867-6>
  75. Weyrich JN, Mason JR, Bazilevskaya EA, Yang H (2023) Understanding the mechanism for adsorption of Pb(II) ions by Cu-BTC metal–organic frameworks. *Molecules* 28:5443. <https://doi.org/10.3390/molecules28145443>
  76. Devi B, Goswami M, Rabha S, Kalita S, Sarma HP, Devi A (2023) Efficacious sorption capacities for Pb(II) from contaminated water: a comparative study using biowaste and its activated carbon as potential adsorbents. *ACS Omega* 8(17):15141–15151. <https://doi.org/10.1021/acsomega.3c00142>
  77. Shikuku VO, Mishra T (2021) Adsorption isotherm modeling for methylene blue removal onto magnetic kaolinite clay: a comparison of two-parameter isotherms. *Appl Water Sci* 11:103. <https://doi.org/10.1007/s13201-021-01440-2>
  78. Wong S, Ghafar NA, Ngadi N et al (2020) Effective removal of anionic textile dyes using adsorbent synthesized from coffee waste. *Sci Rep* 10:2928. <https://doi.org/10.1038/s41598-020-60021-6>
  79. Kuśmierk K, Fronczyk J, Świątkowski A (2023) Adsorptive removal of rhodamine B dye from aqueous solutions using mineral materials as low-cost adsorbents. *Water Air Soil* 234:53. <https://doi.org/10.1007/s11270-023-06511-5>
  80. Amrutha J, Jeppu G, Girish CR et al (2023) Multi-component adsorption isotherms: review and modeling studies. *Environ Process* 10:38. <https://doi.org/10.1007/s40710-023-00631-0>
  81. Abewaa M, Mengistu A, Takele T et al (2023) Adsorptive removal of malachite green dye from aqueous solution using *Rumex abyssinicus* derived activated carbon. *Sci Rep* 13:14701. <https://doi.org/10.1038/s41598-023-41957-x>
  82. Chen H, Qu X, Liu N, Wang S, Chen X, Liu S (2018) Study of the adsorption process of heavy metals cations on Kraft lignin. *Chem Eng Res Des* 139:248–258. <https://doi.org/10.1016/j.cherd.2018.09.028>
  83. Mahamadi C, Nharingo T (2010) Utilization of water hyacinth weed (*Eichhornia crassipes*) for the removal of Pb(II), Cd(II) and Zn(II) from aquatic environments: an adsorption isotherm study. *Environ Technol* 31(11):1221–1228. <https://doi.org/10.1080/09593331003646604>
  84. Qi J, Li Y, Majeed H, Douglas Goff H, Rahman MRT, Zhong F (2019) Adsorption mechanism modeling using lead (Pb) sorption data on modified rice bran-insoluble fiber as universal approach to assess other metals toxicity. *Int J Food Prop* 22(1):1397–1410. <https://doi.org/10.1080/10942912.2019.1650764>
  85. Mahanty B, Behera SK, Sahoo NK (2023) Misinterpretation of Dubinin-Radushkevich isotherm and its implications on adsorption parameter estimates. *Sep Sci Technol* 58(7):1275–1282. <https://doi.org/10.1080/01496395.2023.2189050>
  86. El-Nemr MA, Yılmaz M, Ragab S et al (2023) Isotherm and kinetic studies of acid yellow 11 dye adsorption from wastewater using *Pisum Sativum* peels microporous activated carbon. *Sci Rep* 13:4268. <https://doi.org/10.1038/s41598-023-31433-x>
  87. Neskoromnaya EA, Khamizov RK, Melezhyk AV, Memetova AE, Mkrtchan ES, Babkin, AV (2022) Adsorption of lead ions (Pb<sup>2+</sup>) from wastewater using effective nanocomposite GO/CMC/FeNPs: kinetic, isotherm, and desorption studies. *Colloids and Surfaces A: Physicochemical and Engineering Aspects*, 655, <https://doi.org/10.1016/j.colsurfa.2022.130224>.
  88. Perera GRY, Neetha Dayanthi WKC (2023) Low-cost treatment method for organic matter and nutrients in landfill leachate. *J Water Health* 21(6):789–814. <https://doi.org/10.2166/wh.2023.014>
  89. Chu KH, Bashiri H, Hashim HA, Shukor HYA, Bollinger J (2023) The Halsey isotherm for water contaminant adsorption is fake. *Separation and Purification Technology*, 313, <https://doi.org/10.1016/j.seppur.2023.123500>.
  90. Chu KH, Bashiri H, Hashim MA, Abd Shukor MY, Bollinger J (2023) The Halsey isotherm for water contaminant adsorption is fake. *Separation and Purification Technology*, 313, <https://doi.org/10.1016/j.seppur.2023.123500>.
  91. Gedam VV, Raut P, Chahande A, Pathak P (2019) Kinetic, thermodynamics and equilibrium studies on the removal of Congo red dye using activated teak leaf powder. *Appl Water Science* 9:55. <https://doi.org/10.1007/s13201-019-0933-9>
  92. Wu J, Xia A, Chen C, Feng L, Su X, Wang X (2019) Adsorption thermodynamics and dynamics of three typical dyes onto bio-adsorbent spent substrate of *Pleurotus eryngii*. *Int J Environ Res Public Health* 16(5):679. <https://doi.org/10.3390/ijerph16050679>
  93. Zaid R, Khan SU, Azam A, Farooq IH (2021) A study on effective adsorption of lead from an aqueous solution using copper oxide nanoparticles. *IOP Conf. Ser.: Mater. Sci. Eng.* 1058 012074.
  94. Bidhendi ME, Parandi E, Meymand MM, Sereshti H, Nodeh HR, Joo S, Vasseghian YV, Khatir NM, Rezanian S (2022) Removal of lead ions from wastewater using magnesium sulfide nanoparticles caged alginate microbeads. *Environ Res* 216:1. <https://doi.org/10.1016/j.envres.2022.114416>
  95. Ramos-Guivar JA, Checca-Huaman NR, Litterst FJ, Passamani EC (2023) Surface adsorption mechanism between lead(II, IV) and nanomaghemite studied on polluted water samples collected from the peruvian rivers Mantaro and Cumbaza. *Nanomaterials* 2023(13):1684. <https://doi.org/10.3390/nano13101684>
  96. Tsague CF, Abbo HS, Yufanyi MY, Ondoh AM, Titinchi SJJ (2023) Recyclable functionalized polyethyleneimine-coated magnetic nanoparticles for efficient removal of lead from aqueous solutions. *Chem Technol Biotechnol* 98(8):2023–2038. <https://doi.org/10.1002/jctb.7423>
  97. Jalu RG, Chamada TA, Ramachandran K (2021) Calcium oxide nanoparticles synthesis from hen eggshells for removal of lead (Pb(II)) from aqueous solution. *Environmental Challenges*, 4, <https://doi.org/10.1016/j.envc.2021.100193>
  98. Bayo AB, Amibo TA, Beyan SM (2022) Adsorptive capacity of calcinated hen eggshell blended with silica gel for removal of lead ii ions from aqueous media: kinetics and equilibrium studies. *J Environ Public Health*. 2882546. <https://doi.org/10.1155/2022/2882546>

**Publisher's Note** Springer Nature remains neutral with regard to jurisdictional claims in published maps and institutional affiliations.

Springer Nature or its licensor (e.g. a society or other partner) holds exclusive rights to this article under a publishing agreement with the author(s) or other rightsholder(s); author self-archiving of the accepted manuscript version of this article is solely governed by the terms of such publishing agreement and applicable law.

## Authors and Affiliations

**Nnabuk Okon Eddy<sup>1</sup>**  · **Rajni Garg<sup>2</sup>** · **Richard Alexis Ukpe<sup>3</sup>** · **Paul Ocheje Ameh<sup>4</sup>** · **Rishav Garg<sup>5</sup>** · **Musa Runde<sup>6</sup>** · **Iliya Dimas Kwanchi<sup>6</sup>** · **Saikh Mohammad Wabaidur<sup>7</sup>** · **Sikandar Aftab<sup>8</sup>** · **Raphael Ogbodo<sup>9</sup>** · **Augustine Odiba Aikoye<sup>1</sup>** · **Masoom Siddiqu<sup>8,10</sup>**

✉ Nnabuk Okon Eddy  
okon.nnabuk@unn.edu.ng

Rajni Garg  
rajnigarg@science.org.in

Richard Alexis Ukpe  
ukpera@fuotuo.ke.edu.ng

Paul Ocheje Ameh  
amehpaul199@polac.edu.ng

Rishav Garg  
rishavgarg@science.org.in

Musa Runde  
musa@noun.edu.ng

Iliya Dimas Kwanchi  
kwanchidimas@gmail.com

Saikh Mohammad Wabaidur  
swabaidur@ksu.edu.sa

Sikandar Aftab  
aftab@sejong.ac.kr

Raphael Ogbodo  
ogbodo@uiowa.edu

Augustine Odiba Aikoye  
aikoyeaugustineodiba@gmail.com

<sup>1</sup> Department of Pure and Applied Chemistry, University of Nigeria, Nsukka, Enugu State, Nigeria

<sup>2</sup> Department of Applied Science & Humanities, Galgotias College of Engineering & Technology, Greater Noida 201310, Uttar Pradesh, India

<sup>3</sup> Department of Chemistry, Federal University, Otuoke, Bayelsa State, Nigeria

<sup>4</sup> Department of Chemistry, Nigeria Police Academy, Wudil, Kano State, Nigeria

<sup>5</sup> Department of Civil Engineering, Galgotias College of Engineering & Technology, Greater Noida 201310, Uttar Pradesh, India

<sup>6</sup> Department of Chemistry, National Open University of Nigeria, Jabi, FCT, Abuja, Nigeria

<sup>7</sup> Chemistry Department, College of Science, King Saud University, 11451 Riyadh, Saudi Arabia

<sup>8</sup> Department of Intelligent Mechatronics Engineering, Sejong University, 209 Neungdong-Ro, Gwangjin-Gu, Seoul 05006, South Korea

<sup>9</sup> Department of Chemistry, University of Iowa, Iowa City, IA 52244, USA

<sup>10</sup> Chemistry Department, College of Science, King Saud University, Riyadh, 11451 Riyadh, Saudi Arabia